University of Alberta

High-Resolution MRSI for Radiotherapy Planning

by

Amr Ahmed Heikal

A thesis submitted to the Faculty of Graduate Studies and Research
in partial fulfillment of the requirements for the degree of

Master of Science
in
Medical Physics

Department of Physics

Edmonton, Alberta
Spring 2007

Library and Archives Canada

Published Heritage Branch

395 Wellington Street
Ottawa ON K1A 0N4
Canada

Bibliothèque et Archives Canada

Direction du Patrimoine de l'édition

395, rue Wellington
Ottawa ON K1A 0N4
Canada

Your file Votre référence
ISBN: 978-0-494-29967-8
Our file Notre référence
ISBN: 978-0-494-29967-8

NOTICE:
The author has granted a non-exclusive license allowing Library and Archives Canada to reproduce, publish, archive, preserve, conserve, communicate to the public by telecommunication or on the Internet, loan, distribute and sell theses worldwide, for commercial or non-commercial purposes, in microform, paper, electronic and/or any other formats.

The author retains copyright ownership and moral rights in this thesis. Neither the thesis nor substantial extracts from it may be printed or otherwise reproduced without the author's permission.

AVIS:
L'auteur a accordé une licence non exclusive permettant à la Bibliothèque et Archives Canada de reproduire, publier, archiver, sauvegarder, conserver, transmettre au public par télécommunication ou par l'Internet, prêter, distribuer et vendre des thèses partout dans le monde, à des fins commerciales ou autres, sur support microforme, papier, électronique et/ou autres formats.

L'auteur conserve la propriété du droit d'auteur et des droits moraux qui protège cette thèse. Ni la thèse ni des extraits substantiels de celle-ci ne doivent être imprimés ou autrement reproduits sans son autorisation.

In compliance with the Canadian Privacy Act some supporting forms may have been removed from this thesis.

While these forms may be included in the document page count, their removal does not represent any loss of content from the thesis.

Conformément à la loi canadienne sur la protection de la vie privée, quelques formulaires secondaires ont été enlevés de cette thèse.

Bien que ces formulaires aient inclus dans la pagination, il n'y aura aucun contenu manquant.

Canada

In loving memory of my father,

Ahmed

Abstract

The potential use of high-resolution magnetic resonance spectroscopic imaging (MRSI) for radiotherapy planning is investigated in this thesis. A number of tests are conducted to study the effects of reducing the voxel size in high-resolution MRSI on the spectral signal-to-noise ratio (SNR), and the metabolite ratios. An assessment of the quality of biological tumor delineation using two ranges of resolution in MRSI is conducted using a gelatin phantom designed to eliminate zero-averaging partial volume as well as magnetic susceptibility artifacts. The results show that the decrease in SNR associated with the decrease in voxel size was tolerable and that the metabolite ratios measured with both resolutions agreed within error. The differences in tumor delineation between high- and low-resolution MRSI is demonstrated using the gel phantom. Finally, further uses of gel phantoms are suggested to optimize the parameters used for biological tumor delineation.

Acknowledgments

I would like to dedicate this thesis to the memory of my father, Ahmed. I know this would have made him proud. He has always inspired me in all my life. I aspire to become as great a man, a husband and a father as he was.

To my mother, you have supported me all my life. Although it was and still is very hard for you to see your son live thousands of miles away you have always been supporting and encouraging. You have taken care of all the unfinished business I left back home and have always provided great emotional support. To my wife, Dalia, you truly are the best thing that ever happened to me. You have provided me with enormous support even before we got married. You are the one who convinced me to pursue my dream and not settle for less. You have always been there in the hard times before the good times. You have always believed in me even when it involved starting a new life in a new country. You are one of a kind and no matter how much I write it will never be enough to thank you for what you have done for me.

Dr. Fallone, thank you for accepting me into this program and giving me the chance to change my career and my life. This program was and still is a great experience. Thank you for you support scientifically and financially. You have always provided great supervision, direction and feedback for my work. Dr. Wachowicz, you have played an instrumental role in my thesis work. You have provided excellent feedback and support for my work as well as great insight and supervision. I look forward to working with you in my PhD. Dr. Murray, and Dr. Urtasun, thank you for your support and for

the biological and clinical knowledge you bring to the table. Medical physics is a true interdisciplinary field and your feedback enriched my work.

To my brothers, Khaled and Hesham, I cannot thank you enough. You have been so supportive and encouraging. Unfortunately I don't get to see you often enough yet you are always there when I need you and I truly appreciate our close knit family.

To my friends and office mates, Steven, you are the greatest friend one can have. You are full of energy and ideas and have always provided sound advice and great help. I wish you the best in your defense and your career. I hope we can work together someday. Thalaat, you are truly a great friend. Although we argue a lot you have always been supportive and told me there was light at the end of the tunnel. You were right I see the light. It is an honor to know someone as smart and hardworking as you. My MR buddy, the forever cheerful Lesley, I can't say much more than you always brighten up the office with your music and your attitude, keep it up. Yingli, you are such a hard worker yet every now and then you would crack the most hilarious comment or joke. I look forward to sharing this office with you for a few more years. Sandra, one sentence, I cannot remember the last day you were not smiling. You are a strong person who appreciates friendship and values life. Ryan, Mat and Dave, you guys are great friends that one can depend on in the time of need. Dave I will not miss arguing with you I will however miss your energy. Michael and Ben, we haven't known each other for a long period of time but I can tell you are as great friends are you are physicists.

I would like to thank Dr. Abdulkarim, Dr. Pervez and Dr. Sinha for their work in the GBM study. You have supplied me with the priceless clinical information and the chance to apply our research on clinical subjects.

Finally to all Medical Physics, Physics and Oncology professors and staff, thank you for making this program as great as it is. This experience wouldn't have been as great as it was without you.

CHAPTER ONE 1

1 INTRODUCTION 1

1.1 INTRODUCTION: 1
1.2 IMAGING AND THE RADIOTHERAPY PROCESS: 2
1.2.1 Diagnostic and 3-D Imaging: 3
1.2.2 MRI and Tumor Delineation: 4
1.2.3 MRI vs. CT: 6
1.3 TREATMENT PLANNING: 7
1.4 TREATMENT DELIVERY: 8

CHAPTER TWO 14

2 THEORY OF MAGNETIC RESONANCE SPECTROSCOPY 14

2.1 CHEMICAL SHIFT IMAGING (MR SPECTROSCOPY): 14
2.2 LOCALIZATION TECHNIQUES OF MRS: 16
2.2.1 Stimulated Echo acquisition Mode (STEAM): 16
2.2.2 Point Resolved Spectroscopy (PRESS): 17
2.2.3 Spectroscopic Imaging (SI): 19
2.3 SIGNAL AND NOISE CONSIDERATIONS: 21
2.3.1 Signal: 22
2.3.2 Noise: 23
2.3.3 Signal-to-Noise Ratio (SNR): 25

CHAPTER THREE 28

3 ASSESSMENT OF BIOLOGICAL TUMOR DELINEATION USING A GEL PHANTOM 28

3.1 INTRODUCTION: 28
3.2 MATERIALS AND METHODS: 30
3.2.1 Spectroscopic Imaging Scan: 32
3.2.1.1 Nominal Spatial Resolution: 35
3.2.1.2 Effective Voxel Size: 36
3.2.1.3 Field of View (FOV): 36
3.2.1.4 Volume of Interest (VOI): 36
3.2.1.5 Shimming: 37
3.2.1.6 Aliasing (fold-over) artifacts: 39
3.2.1.7 Water Suppression: 40
3.2.2 Processing: 41
3.2.3 Phantom Studies: 45
3.2.3.1 Spectral SNR study: 45
3.2.3.2 Effects of Voxel Size on Metabolite Ratios: 48
3.2.4 Comparison of High-Resolution with Low-Resolution MRSI: 49
3.2.5 Volunteers and Clinical Subject Studies: 53
3.3 RESULTS: 54
3.3.1 SNR Study 57
3.3.2 Effects of Voxel Size on Metabolite Ratios 60
3.3.3 Clinical Subject Studies 61
3.3.4 Comparison of High-Resolution vs. Low-Resolution MRSI 62

CHAPTER FOUR 70

4 CONCLUSIONS AND FUTURE WORK 70

4.1 CONCLUSIONS: 70

4.2 FUTURE WORK: 72

BIBLIOGRAPHY 75

APPENDIX I: THEORY OF MRI 82

INTRODUCTION: 82
QUANTUM MECHANICAL DESCRIPTION OF NMR 82
Spin ½ in a static magnetic field (preparation): *82*
THE CLASSICAL DESCRIPTION OF NMR: 86
Magnetic moments in a stationary magnetic field B_0: *86*
Description of the excitation process: *87*
Description of the signal-inducing excited state: *94*
RELAXATION MECHANISMS AND THE BLOCH EQUATIONS: 97
Longitudinal relaxation: *97*
Transverse Relaxation: *101*
SPATIAL ENCODING: 103
Slice Selection: *105*
Frequency Encoding: *105*
Phase Encoding: *107*
Radio-Frequency excitation pulses: *108*
THE SIGNAL EQUATION: 110

APPENDIX II: PEAK FITTING ALGORITHM 115

List of Tables

Table (A-1): T1 Value Of Different Tissue At 1.5T And 3T. 98

Table (A-2): T2 values for brain tissue at 1.5 T. 101

List of Figures

Figure (2-1): *Schematic for a STEAM sequence.* 17

Figure (2-2): *Schematic of a PRESS Sequence.* 18

Figure (2-3): *A schematic of a 2-D PRESS sequence.* 21

Figure (3-1): *A schematic of a multi-slice MRSI sequence with TSI turbo factor of 2. TE_1 and TE_2 are the first and second echo times respectively.* 34

Figure (3-2): *A typical spectrum showing the NAA, Cho, and Cr peak. The blue line represents the raw spectrum while the red line represents the fitted spectrum. The under shooting in the raw spectrum at approx. 2.1 and 2.3 ppm is caused by noise and ringing artifacts.* 42

Figure (3-3): *Typical Spectra individually scaled from SNR study. (a) 10×10×10 mm^3/voxel scan, (b) 5×5×10 mm^3/voxel scan, (c) 4.25×4.24×10 mm^3/voxel scan ,and (d) 3.33×3.33×10 mm^3/voxel scan. The displayed window is the noise window.* 47

Figure (3-4): *Creatine metabolite map of the uniform phantom showing the ROI used for the SNR and metabolite ratio studies.* 48

Figure (3-5): *T2 weighted transverse image of the wedge phantom. The dashed lines outline the wedge. The dimensions shown are smaller than the ones quoted due to the partial immersion of the wedge in the gel.* 50

Figure (3-6): *Cho/Cr ratio map of the phantom with a contour (black) at Cho/Cr = 1.75. The image is masked around the VOI.* 53

Figure (3-7): *The Spectroscopic Imaging grids (FOVs) for (a) the low–resolution (9.5×9.5×10 mm^3/voxel) scan (b) the high-resolution (5.83×5.83×10mm^3/voxel) scan. VOI shown as the green shaded region in the centre.* 55

Figure (3-8): *SNR study results. (a) Phantom (10×10×10 mm^3/voxel). (b) Phantom (5×5×10 mm^3/voxel). (c) Phantom (4.17×4.17×10 mm^3/voxel). (d) Phantom (3.33×3.33×10 mm^3/voxel). (e) Volunteer low resolution (9.58×9.58×10 mm^3/voxel). (f) Volunteer high resolution (5.83×5.83×10 mm^3/voxel). (g) Volunteer high resolution (5×5×10 mm^3/voxel). The left vertical scale corresponds to the bar graph representing the SNR, while the right vertical scale corresponds to the line graph representing the number of standard deviations separating the mean Cr height and mean noise level.* 56

Figure (3-9): *Volunteer creatine maps acquired with TR 1200 ms at (a) high-resolution (6.25×6.25×10mm^3/voxel) and (b) low-resolution (10×10×10mm^3/voxel). The maps are scaled individually and the colorbar represents relative intensity. The arrow identifies the ventricles.* 57

Figure (3-10): *SNR study results. (a) Phantom (10×10×10 mm^3/voxel). (b) Phantom (5×5×10 mm^3/voxel). (c) Phantom (4.17×4.17×10 mm^3/voxel). (d) Phantom (3.33×3.33×10 mm^3/voxel). (e) Volunteer low resolution (9.58×9.58×10 mm^3/voxel). (f) Volunteer high resolution (5.83×5.83×10 mm^3/voxel). (g) Volunteer high resolution (5×5×10 mm^3/voxel). The left vertical scale corresponds to the bar graph which represents the SNR, while the right vertical scale corresponds to the line graph which represents the number of standard deviation between the mean creatine peak height and the mean noise.* 59

Figure (3-11): *Typical spectrum from the uniform phantom used for the SNR and metabolite ratio studies. The peaks of interest are Cho and Cr at 3.2 ppm and 3.0 ppm respectively.* 60

Figure (3-12): *Effects of voxel size on metabolite ratios.* 61

Figure (3-13): *(a) T1-weighted post-contrast image of a clinical GBM subject post-surgery. (b) MRSI spectra corresponding to a clinical GBM subject. Spectrum #1 corresponds to a point inside the tumor as shown by the contrast enhancement in the anatomic image. Spectrum #2 corresponds to a point within the healthy tissue.* 62

Figure (3-14): *Comparison of the spectroscopic scan mask at Cho/Cr ratio of 1.75 to the anatomic (actual) scan of the wedge phantom. (a) High-resolution (5×5×10 mm^3/voxel) scan. (b) Low-resolution (10×10×10 mm^3/voxel) scan. Notice the difference in phantom coverage especially in the high detail region of the phantom. Also notice the blurring and over estimation of the phantom size in the low detail region.* 64

Figure (3-15): *Bar graph comparing the results of the quantitative comparison between high-resolution (5×5×10 mm^3/voxel) and low-resolution (10×10×10 mm^3/voxel) scans of the wedge phantom. Notice the high-resolution scans always yield less misses and excess pixels than the low-resolution scans at all thresholds.* 65

Figure (3-16): *5% by weight porcine gel wedge phantom. Comparison of the spectroscopic scan mask at Cho/NAA ratio of 1 to the anatomic (actual) scan of the wedge phantom. (a) High-resolution (5×5×10 mm^3/voxel) scan. (b) Low-resolution (10×10×10 mm^3/voxel) scan. The high resolution was scanned first then the low resolution followed after 5 minutes.* 66

Figure (3-17): *15% by weight porcine gel wedge phantom. Comparison of the spectroscopic scan mask at Cho/NAA ratio of 1 to the anatomic (actual) scan of the wedge phantom. (a) High-resolution (5×5×10 mm^3/voxel) scan. (b) Low-resolution (10×10×10 mm^3/voxel) scan. The low resolution was scanned first then the high resolution followed after 5 minutes.* 67

Figure (A-1): *The energy level diagram of a spin ½ system observed in $B_0 = 0$ and $B_0 \neq 0$.* 85

Figure (A-2): *Magnetic moment vector within a sample shown in: (a) The absence of a uniform external magnetic field resulting in random orientations zero net magnetization. (b) The magnetic moments are arranged in the parallel and anti-parallel orientation with respect to the applied magnetic field. The net magnetization vector M_0 resulting is shown as the big arrow.* 87

Figure (A-3): *The rotating frame of reference ($X_\rho Y_\rho$) with respect to the laboratory frame (X,Y).* 90

Figure (A-4): *The magnetization vector precession about B_{eff} in the rotating reference frame.* 92

Figure (A-5): *The motion of the magnetization vector during a 90° excitation pulse shown in a. the laboratory frame and b. the rotating frame.* 93

Figure (A-6): *Magnetization vector M_0 precessing in a negative sense about the z-axis in the presence of a static magnetic field B_0 applied along the z-direction.* 96

Figure (A-7): *(a) The time domain induced e.m.f in the coil and (b) frequency profile of the detected signal- (Ignoring relaxation).* 97

Figure (A-8): *Longitudinal relaxation of white matter at 3T following a 90° pulse and a 180° pulse.* 100

Figure (A-9): *Longitudinal relaxation of white matter and grey matter at 3T following a 90° pulse.* 100

Figure (A-10): *Fluctuations in ω_0 resulting in phase spread and loss of coherent signal.* 102

Figure (A-11): *A description of the application of magnetic field gradients for spatial encoding.* 104

Figure (A-12): *A typical hard pulse as shown in a. time domain and (b) frequency domain.* 109

Figure (A-13): *An ideall soft pulse as shown in a. time domain and b frequency domain.* 110

Figure (A-14): *(a) Schematic of a gradient echo sequence. (b) The k-space sampling trajectory caused by the application of the gradients in the sequence.* 112

List of Abbreviations

2-D PRESS	Two-Dimensional Point Resolved Spectroscopy
3-D PRESS	Three-Dimensional Point Resolved Spectroscopy
BTV	Biological Target Volume (BTV)
CHESS	Chemical Shift Selective
Cho	Choline
CNI	Choline-to-NAA Index
CTV	Clinical Target Volume
CT	Computed Tomography
Cr	Creatine
DSA	Digital Shift Accumulation
FID	Free Induction Decay
fMRI	Functional MRI
FOV	Field-of-View
FWHM	Full Width at Half Maximum
GBM	Glioblastoma Multiforme
GTV	Gross Tumor Volume
HT	Helical Tomotherapy
IMRT	Intensity Modulated Radiotherapy
k-space	Spatial Frequency Space
MRI	Magnetic Resonance Imaging
MRS	MR Spectroscopy
MRSI	Magnetic Resonance Spectroscopic Imaging

NAA	N-acetylaspartate
NTCP	Normal Tissue Complication Probability
PET	Positron Emission Tomography
PRESS	Point Resolved Spectroscopy
PTV	Planning Target Volume
SESI	Spin Echo Spectroscopic Imaging
SNR	Signal-to-Noise Ratio
SPECT	Single Photon Emission Computed Tomography
STEAM	Stimulated Echo Acquisition Mode
TCP	Tumor Control Probability
TE	Echo Time
TR	Repetition Time
TSE	Turbo Spin Echo
TSI	Turbo Spectroscopic Imaging
RMS	Root-Mean-Square
ROI	Region-of-Interest
RF	radio-frequency
US	Ultra-Sound
VOI	Volume-of-Interest

Chapter One

1 Introduction

1.1 Introduction:

When an individual is diagnosed with cancer there are usually three treatment options: surgery, radiotherapy, and chemotherapy. For most solid tumors the initial method of treatment is surgical excision. However, combined modality treatments are routinely used to improve the probability of tumor control. For instance, Glioblastoma Multiforme (GBM) is usually treated with surgery followed by radiotherapy and chemotherapy.[1-3] As studies have shown, this leads to a significant improvement in tumor control.[2-4]

The radiotherapy process consists of a series of stages that start with the patient being diagnosed with a tumor and ends with patient follow-up after treatment. The process can be resembled by a chain that is as strong as its weakest link. The links on the chain are; tumor definition, treatment planning and dose delivery.[5] With advancements in treatment planning and dose delivery systems, tumor definition (delineation) has become the stage most in need of refinement. Microscopic disease outside of the gross tumor volume is hard to detect using conventional imaging techniques. Accordingly, a large portion of tumor recurrences, e.g GBM, are attributed to undetected (untreated) microscopic disease.[6-9] Magnetic Resonance Spectroscopic Imaging (MRSI) and Positron Emission Tomography (PET) have been suggested as biological imaging

modalities that may be able to detect microscopic disease.[10-14] Incorporating those biological modalities in the radiotherapy process can lead to improved biological delineation of the tumors which may in turn lead to the reduction of microscopic disease related recurrences.[15-17]

This thesis will discuss the improvements that can be introduced to biologically based tumor delineation using MRSI. This chapter discusses the role of imaging in the radiotherapy process, specifically, the role MRI and MRSI play in tumor delineation. It also briefly discusses some of the basics of contouring and the advancements in treatment delivery that led to the increasing importance of biological imaging in solid tumors.

1.2 Imaging and the Radiotherapy Process:

Imaging is essential to the radiotherapy processes especially in the case of solid tumors as it is involved in a number of its stages. Firstly, imaging usually plays a role in the diagnosis and the prognosis of cancer. Secondly, when radiotherapy is the treatment of choice, 3-D imaging becomes important for tumor delineation, organ localization and dose calculations. Finally, portal imaging is used for position verification and in some cases dose reconstruction. This section briefly describes the uses of different imaging modalities in the diagnosis and treatment planning of cancer.

1.2.1 Diagnostic and 3-D Imaging:

Imaging modalities can be divided into two main categories; anatomic and functional modalities. Anatomic modalities such as X-Ray, Computed Tomography (CT), Magnetic Resonance Imaging (MRI) and Ultra-Sound (US) provide images of anatomic structures. They rely on different techniques for imaging the anatomic structures and can sometimes indicate the functionality of an organ. However, anatomic modalities are generally unable to detect metabolic or biochemical changes within tissue.

On the other hand, functional and metabolic modalities such as Positron Emission Tomography (PET), Single Photon Emission Computed Tomography (SPECT), functional MRI (fMRI) and MR Spectroscopic Imaging (MRSI) provide images of the metabolism or functionality of different organs. Those modalities depend on either radiopharmaceutical uptake in the case of PET and SPECT, changes in blood oxygenation levels for fMRI or on biochemical compositions within the imaged body as in MRSI.

The most commonly used modality in the radiotherapy process is CT. Besides being a good diagnostic imaging modality, generally having high-spatial resolution and short scan times, CT is of specific importance to the radiotherapy process as its images provide the electron density information necessary for dose calculations. Accordingly, a planning CT is used as the basis for most radiotherapy treatment planning.

CT provides excellent contrast between soft tissue, bony structures and air due to its dependence on x-ray attenuation coefficients for contrast. However, contrast within the soft tissue (soft tissue contrast) is poor in CT due to the similarity of the attenuation coefficients within soft tissue. Thus, relying on CT alone for tumor delineation and organ localization in soft tissue might lead to poor boundary definitions due to the reduced contrast. As a result, CT is routinely used with other higher soft tissue contrast modalities for tumor delineation and organ localization.

1.2.2 MRI and Tumor Delineation:

CT relies on the difference in the x-ray attenuation coefficients in the imaged body to produce contrast. Contrast can be enhanced by using different x-ray energies or by using a contrast agent. The contrast agent is a high electron density material that is usually injected or swallowed by the patient. The agent is then imaged directly by CT.

Because MRI most commonly relies on hydrogen protons for signal, it may appear that the only source of contrast in MRI is proton density. In that case it is not much different from CT which relies on electron density for contrast. However, MRI can detect subtle changes in tissue caused by changes in anatomy or the surrounding chemistry. Such changes can manifest themselves as changes in relaxation times. That difference in relaxation is the most used contrast mechanism in MRI.

Differences in relaxation arise from the differences in chemical composition between tissue types.(see *Appendix I* for the explanation of relaxation mechanisms in

MRI) Those changes in the relaxation can be detected in MRI and used for contrast. By optimizing the scan parameters, the relative signal received from different tissues can be changed. In the case of the brain, without the use of any contrast agents, white matter would appear brighter than grey matter on T1 weighted images, while on T2 weighted images white matter would appear darker than grey matter. There are also techniques to suppress or enhance the signal of certain compounds (e.g. water and fat) without the need of contrast agents. Sources of contrast in MRI are not limited to relaxation. Other sources of contrast include diffusion, perfusion, and magnetization transfer which is used for non-invasive angiography.

In GBM studies, MRI scans are routinely used for treatment planning.[15, 16] T2 weighted scans show the extent of the tumor and the surrounding edema while contrast enhanced T1 weighted scans are the most commonly used for tumor delineation. Due to the breakage of the blood brain barrier caused by the tumor, the contrast agent in the blood stream enhances the appearance of the tumor while the surrounding edema and necrosis are left un-enhanced, providing very high contrast. Also, MRI diffusion and perfusion studies can be performed to define and evaluate tumor malignancy and stage.[18]

The same scanners used for MRI are able to perform biochemical imaging in the form of MRS. MRS relies on the chemical shift phenomenon to distinguish between different chemical compounds in the same way an *in-vitro* NMR experiment would.

Combined with spatial encoding, MRS can be transformed to MRSI where an image can be produced describing the biochemical composition of the imaged subject.

1.2.3 MRI vs. CT:

In radiotherapy treatment planning, the electron density of tissue is important in order to perform correct dose calculations. CT relies on differences in x-ray attenuation coefficients for contrast. The attenuation coefficients of materials being imaged are converted into electron density which provides the necessary information for dose calculations. Therefore, it is very hard to replace CT with MRI as the main modality used in treatment planning. It is in the versatility of MRI that its strength lies. A single MR study can be used to produce multiple contrast anatomic images along with biochemical information that can potentially be used for biological assessment. [18]

Combining the excellent soft tissue contrast of MRI for better tumor delineation with the electron density information provided by CT for dose calculations can lead to more conformal plans compared to using CT alone. Furthermore, the use of MRSI adds the dimension of biological targeting to the otherwise purely anatomically based tumor delineation. Image registration techniques such as slice alignment using fiducial makers, or mutual information are used to fuse CT images with their corresponding MRI and MRSI counterparts. The resulting fused images are used in the treatment planning system for tumor delineation, organ localization and dose calculations.[17]

1.3 Treatment Planning:

The goal of radiotherapy is to deliver a prescribed dose of radiation to the tumor while minimizing the dose delivered to the surrounding normal tissue. To achieve this goal a treatment plan is developed in which the target tumor volume as well as the organs at risk are contoured. Those volumes are contoured using the images acquired in the previous 3-D imaging stage. Accordingly, the quality of those images, whether anatomic or biochemical, affects the target contours and in turn the outcome of the treatment.

As mentioned above, the treatment plan involves volume contouring. During this stage a series of volumes are defined to guide the plan. Generally, three contours are used to define the target for radiation; the gross tumor volume (GTV), the clinical target volume (CTV), and the planning target volume (PTV). The GTV is usually contoured by the clinician and is defined by the boundaries of the visible tumor on the anatomic scan. In GBM the GTV is defined on the T1 contrast enhanced images by the boundaries of contrast enhancement (edge enhancement). The CTV includes the GTV and extends beyond it to include possible regions of microscopic disease. The margin between GTV and CTV varies according to the tumor site and stage. For GBM the margin between GTV and CTV is 2 cm and it is here that some recurrences occur.[7, 8, 19] PTV is then defined to include both GTV and CTV and is the main target for treatment planning. PTV is larger than CTV and it accounts for setup errors and patient movement. The margin of PTV usually doesn't exceed 5 mm depending on the tumor site, the immobilization devices, the reproducibility of patient setup and organ movements.[7, 8] The PTV is the volume to which the prescribed dose is to be delivered.

One may add two more volumes; the irradiated volume (IV) and the biological target volume (BTV).[5, 14] Although not used in the initial planning, the IV represents the actual irradiated volume for a beam selection. The IV is always larger than the desired PTV due to build up and exit doses. In the beam selection and optimization stage which follows target definition, the treatment planning goal is to reduce the dose to normal tissue within the IV in order to reduce complications.

Unlike the previously mentioned GTV, the BTV is defined using biochemical or functional modalities.[14] It outlines regions of tumor activity and is interpreted differently depending on the tumor type and stage.[14] In some cases the BTV can be used to define dose boost volumes or nonuniform margins for tumor extent and microscopic disease.[11]

Following target definition, the treatment protocol and beam arrangements are selected. Dose calculations are performed and the treatment plan is optimized for the goals of the treatment.

1.4 Treatment Delivery:

Delivering radiation therapy can be done using two commonly used techniques: external beam radiotherapy using x-ray or gamma ray emitting units, or brachytherapy using sources placed inside or in close proximity to tumors. Only advancements in external beam radiotherapy will be discussed in this section.

External beam radiation devices range from kilo-voltage (kV) x-ray units that are used for superficial treatments through cobalt units and linear accelerators (linacs). With the exception of Cobalt units, all external beam radiotherapy units rely on producing x-rays through bremsstrahlung. Electrons are accelerated and focused on a lead/tungsten target which causes them to decelerate rapidly and thereby to produce x-rays, hence the name. In kV units the electrons are accelerated using conventional x-ray tubes. However, in the linacs, due to the high electron energies needed, the electron acceleration process is achieved using high frequency wave guides that differ in design according to the manufacturers.

Some of the most notable advancements in treatment delivery are beam shaping devices. The introduction of multi-leaf collimators has led to the development of Intensity M[illegible]ted Radiotherapy (IMRT). The ability to modulate the dose within the PTV provides the opportunity of dose boosting to the BTV.

Portal imaging devices and on-board imagers outfitted to linacs as well as mega-voltage CT on Helical Tomotherapy (HT) units are readily used for setup verification purposes. However, there is great potential for utilizing those devices for Image Guided Adaptive Radiotherapy in which the treatment plan is adjusted on a dose-to-dose basis to compensate for organ movements and previous setup errors.

All the above mentioned advancements in treatment delivery have had a great influence on either improving the outcome or reducing the toxicity of radiotherapy.[20-23] Novel planning techniques and algorithms combined with IMRT and HT have all provided the means of producing and in most cases delivering a treatment plan that is very conformal to the PTV. This leads to treatments that can be tailored to boost dose to the predefined margins within the tumor while sparing radiosensitive organs, hence, improving tumor control probability and minimizing normal tissue complications.

With the advancements of delivery techniques it has become clear that tumor definition is currently one of the most important links in the radiotherapy process. The GTV for most tumors is usually visible using conventional anatomic imaging modalities. It is the microscopic extent and the biological activity of the tumors that those modalities fail to detect (e.g. in GBM most recurrences arise within 2 cm from the visible GTV). Using a biochemical imaging modality to probe metabolite concentrations that can be linked to tumor growth and characterization a BTV has been added to the delineation stage.

MRSI is a multi-voxel non-invasive biochemical imaging modality that can be used for this purpose. It has been shown that MRSI can be used to probe different metabolite concentrations in the brain and the prostate. Those studies have been correlated with physical biopsies taken from tumor sites.[9, 11, 15, 17, 18]

The purpose of this thesis is to present a phantom based method for the quantitative comparison of MRSI based tumor delineation margins using different spatial resolutions. Chapters Two discusses the theory of MRSI while Chapter Three discusses our experiments and the materials and methods used along with the results achieved. Finally, Chapter Four outlines the conclusions and suggestions for future work. Also, Appendix I that discusses the basic theory of MRI required for the understanding of this thesis and Appendix II that shows the programming code used for the peak fitting algorithm, are provided at the end of the thesis.

References:

1. Brandes, A., Soesan, M., Fiorentino, M.V., *Medical treatment of high grade malignant gliomas in adults: an overview.* Anticancer Res, 1991. **11**(2): p. 719-727.
2. Kristiansen, K., Hagen, S., Kollevold, T., Torvik, A., Holme, I., Nesbakken, R., Hatlevoll, R., Lindgren, M., Brun, A., Lindgren, S., Notter, G., Andersen, A.P., Elgen, K., *Combined modality therapy of operated astrocytomas grade III and IV. Confirmation of the value of postoperative irradiation and lack of potentiation of bleomycin on survival time: a prospective multicenter trial of the Scandinavian Glioblastoma Study Group.* Cancer, 1981. **47**(4): p. 649-653.
3. Lassen, U., Kristjansen, P.E., Wagner, A., Kosteljanetz, M., Poulsen, H.S., *Treatment of newly diagnosed glioblastoma multiforme with carmustine, cisplatin and etoposide followed by radiotherapy. A phase II study.* J Neurooncol., 1999. **42**(2): p. 161-166.
4. Fine, H.A., Dear, K.B., Loeffler, J.S., Black, P.M., Canellos, G.P., *Meta-analysis of radiation therapy with and without adjuvant chemotherapy for malignant gliomas in adults.* Cancer, 1993. **71**(8): p. 2585-2597.
5. Van Dyk, J., *The Modern Technology of Radiation Onocology.* 1999: Medical Physics Publishing.
6. Alexander, E.r., Loeffler, J.S., *Radiosurgery for primary malignant brain tumors.* Semin. Surg. Oncol., 1998. **14**(1): p. 43-52.
7. Hess, C.F., Schaaf, J.C., Kortmann, R.D., Schabet, M., Bamberg, M., *Malignant glioma: patterns of failure following individually tailored limited volume irradiation.* Radiother. Oncol., 1994. **30**(2): p. 146-149.
8. Lee, S.W., Fraass, B.A., Marsh, L.H., Herbort, K., Gebarski, S.S., Martel, M.K., Radany, E.H., Lichter, A.S., Sandler, H.M., *Patterns of failure following high-*

dose 3-D conformal radiotherapy for high-grade astrocytomas: a quantitative dosimetric study. Int. J. Radiat. Oncol. Biol. Phys., 1999. **43**(1): p. 79-88.

9. Wallner, K.E., Galicich, J.H., Krol, G., Arbit, E., Malkin, M.G., *Patterns of failure following treatment for glioblastoma multiforme and anaplastic astrocytoma.* Int. J. Radiat. Oncol. Biol. Phys., 1989. **16**(6): p. 1405-1409.
10. Kwee, S.A., Coel, M.N., Lim, J., Ko, J.P., *Combined use of F-18 fluorocholine positron emission tomography and magnetic resonance spectroscopy for brain tumor evaluation.* J. Neuroimaging, 2004. **14**(3): p. 285-289.
11. Pirzkall, A., Li, X., Oh, J., Chang, S., Berger, M.S., Larson, D.A., Verhey, L.J., Dillon, W.P., Nelson, S.J., *3D MRSI for resected high-grade gliomas before RT: tumor extent according to metabolic activity in relation to MRI.* Int. J. Radiat. Oncol. Biol. Phys., 2004. **59**(1): p. 126-137.
12. Walecki, J., Tarasow, E., Kubas, B., Czemicki, Z., Lewko, J., Podgorski, J., Sokol, M., Grieb, P., *Hydrogen-1 MR spectroscopy of the peritumoral zone in patients with cerebral glioma: assessment of the value of the method.* Acad. Radiol., 2003. **10**(2): p. 145-153.
13. Pallud, J., Devaux, B., Nataf, F., Roux, F.X., Daumas-Duport, C., *Spatial delimitation of low grade oligodendrogliomas.* Neurochirurgie. , 2005. **51**(3-4): p. 253-259.
14. Ling, C.C., Humm, J., Larson, S., Amols, H., Fuks, Z., Leibel, S., Koutcher, J.A., *Towards multidimensional radiotherapy (MD-CRT): biological imaging and biological conformality.* Int. J. Radiat. Oncol. Biol. Phys. , 2000. **47**(3): p. 551-560.
15. Nelson, S.J., Graves, E., Pirzkall, A., Li, X., Chan, A.A., Vigneron, D.B., McKnight, T.R., *In Vivo molecular imaging for planning radiation therapy of gliomas: an application of 1H MRSI.* J. Magn. Reson. Imaging., 2002. **16**(4): p. 464-476.
16. McKnight, T.R., Noworolski, S.M., Vigneron, D.B., Nelson, S.J., *An automated technique for the quantitative assessment of 3D-MRSI data from patients with glioma.* J. Magn. Reson. Imaging., 2001. **13**(2): p. 167-177.
17. Chang, J., Thakur, S., Perera, G., Kowalski, A., Huang, W., Karimi, S., Hunt, M., Koutcher, J., Fuks, Z., Amols, H., Narayana, A., *Image-fusion of MR spectroscopic images for treatment planning of gliomas.* Med. Phys., 2006. **33**(1): p. 32-40.
18. Di Costanzo, A., Scarabino, T., Trojsi, F., Giannatempo, G.M., Popolizio, T., Catapano, D., Bonavita, S., Maggialetti, N., Tosetti, M., Salvolini, U., d'Angelo, V.A., Tedeschi, G., *Multiparametric 3T MR approach to the assessment of cerebral gliomas: tumor extent and malignancy.* Neuroradiology, 2006. **48**(9): p. 622-631.
19. Kantor, G., Loiseau, H., Vital, A., Mazeron, J.J., *Gross tumor volume (GTV) and clinical target volume (CTV) in adult gliomas.* Cancer Radiother., 2001. **5**(5): p. 571-580.
20. Zelefsk, M.J., Chan, H., Hunt, M., Yamada, Y., Sippy, A.M., Amols, H., *Long-term outcome of high dose intensity modulated radiation therapy for patients with clinically localized prostate cancer.* J. Urol., 2006. **176**(4): p. 1415-1419.

21. Fuller, C.D., Thomas, C.R.J., Wong, A., Cavanaugh, S.X., Salter, B.J., Herman, T.S., Fuss, M., *Image-guided intensity-modulated radiation therapy for gallbladder carcinoma.* Radiother. Oncol., 2006. **81**(1): p. 65-72.
22. Combs, S.E., Konkel, S., Schulz-Ertner, D., Munter, M.W., Debus, J., Huber, P.E., Thilmann, C., *Intensity modulated radiotherapy (IMRT) in patients with carcinomas of the paranasal sinuses: clinical benefit for complex shaped target volumes.* Radiat. Oncol., 2006. **1**: p. 23.
23. Rades, D., Fehlauer, F., Wroblesky, J., Albers, D., Schild, S.E., Schmidt, R., *Prognostic factors in head-and-neck cancer patients treated with surgery followed by intensity-modulated radiotherapy (IMRT), 3D-conformal radiotherapy, or conventional radiotherapy.* Oral Oncol., 2006. doi:10.1016/j.oraloncology.2006.05.006.

Chapter Two

2 Theory of Magnetic Resonance Spectroscopy

2.1 Chemical shift imaging (MR spectroscopy):

Magnetic resonance imaging is based on imaging primarily water protons, as it is the most abundant molecule in the human body, and relies heavily on differences in relaxation times as a source of contrast. However, the original NMR experiments were essentially spectroscopy experiments. As opposed to imaging which relies on all protons having the same resonance frequency, MR spectroscopy (MRS) exploits the chemical shift phenomenon to detect different chemical compositions within a sample.

Since atoms are the building blocks of molecules, nuclei within those atoms are affected by the distribution of electrons in the chemical bond in the molecule. That distribution of electrons affects the resonance frequency of the protons in the molecule. This dependence of the resonance frequency on the molecular structure compared to a water proton is known as the chemical shift.

Nuclei within the molecules are shielded from the static magnetic field B_0 through the electron cloud surrounding them. According to Lenz's law, due to circulation induced by B_0 in the electron cloud, a magnetic field B_i is induced by the electron cloud to oppose the circulation from B_0. The induced field B_i has a

magnitude that is proportional to the original field B_0 and a direction opposite to B_0, thus:

$$B_{local} = B_0 - B_i . \qquad (2\text{-}1)$$

The induced field is directly proportional to the applied field with the constant of proportionality being σ, the shielding constant. σ is unique to the local environment of the nucleus.[1] Therefore Eq. 2-1 becomes

$$B_{local} = B_0(1-\sigma) \qquad (2\text{-}2)$$

Therefore, the precession frequency ω of those protons is: (see *Appendix I* Eq. A-6 and Eq. A-7 for details)

$$\omega = \gamma B_0(1-\sigma) . \qquad (2\text{-}3)$$

where γ is the gyromagnetic ratio and is equal to 6.796 radians/(second · Tesla).

Accordingly, the frequency shift between the protons in different electronic environments is dependent on the applied magnetic field; the larger the field, the larger the shift. Therefore the use of high fields would improve peak separation and spectral resolution as well as the SNR as shown in the following sections.

Due to the dependence of the chemical shift frequency on the applied field, the parts-per-million (ppm) , δ, scale is used as a normalized measure of chemical shift.[1]

$$\delta = \frac{\omega_{molecule} - \omega_{reference\ molecule}}{\omega_{reference\ molecule}} \times 10^6\ ppm \qquad (2\text{-}4)$$

Most relevant metabolites of interest *in-vivo* are in the range of 1-4.7 ppm. Such range corresponds to a frequency spread of approximately 473 Hz and 236 Hz at 3T and 1.5T respectively.

2.2 Localization Techniques of MRS:

For single voxel spectroscopy, localization of the source of the signal is important. The most popular techniques for localization involve applying three RF pulses on the three orthogonal planes, where the intersection of the planes defines the voxel from which the signal is acquired. (see *Appendix I* for details on spatial encoding and slice selection) Stimulated Echo Acquisition Mode (STEAM) and Point Resolved Spectroscopy (PRESS) are the most popular spectroscopy of those pulse sequences that utilize this method of localization.

2.2.1 Stimulated Echo acquisition Mode (STEAM):

STEAM uses three 90° excitation pulses applied on the three orthogonal planes. The three excitation pulses generate a stimulated echo only at the intersection

of the three planes therefore acquiring the signal from the defined cube.[2] Echo time (TE) is independent of the mixing time (TM) between the second and the third pulse. Accordingly, TM can be adjusted and the overall scan time can be reduced significantly.

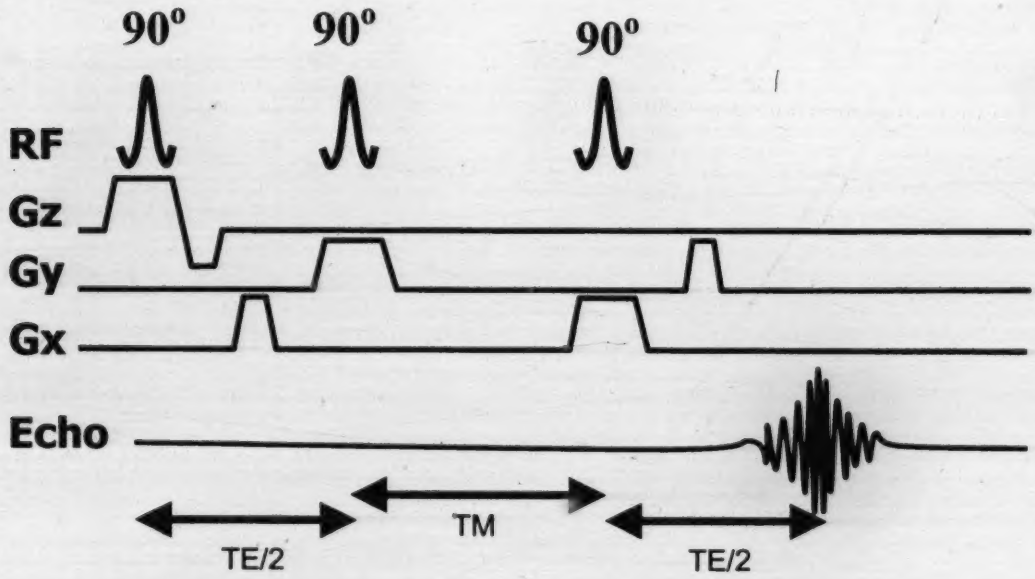

Figure (2-1): Schematic for a STEAM sequence. The three 90° excitation pulses applied on the three orthogonal planes define a volume of interest (voxel) from which the signal is acquired.

2.2.2 Point Resolved Spectroscopy (PRESS):

Similar to STEAM, PRESS relies on three RF pulses. However, in the case of PRESS, the first 90° excitation pulse is followed by two 180° pulses generating an spin echo at the intersection of the 3 planes on which they are applied.[3-5]

PRESS and STEAM each have different advantages and disadvantages. STEAM permits the detection of metabolites with shorter T2 relaxation due to its shorter TE compared to PRESS. However, PRESS inherently has a higher SNR due to the inherent loss of signal in the stimulated echoes.

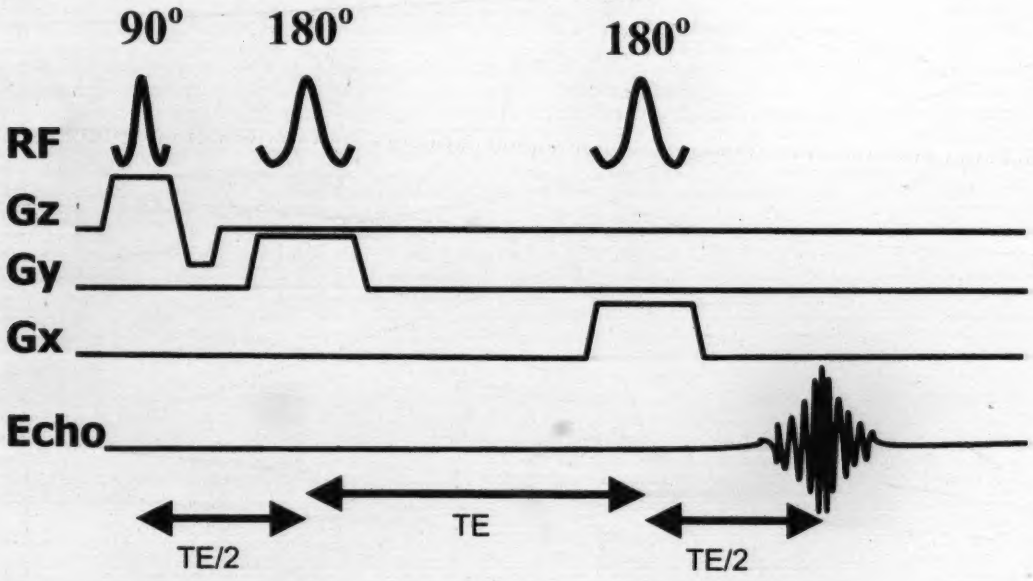

Figure (2-2): Schematic of a PRESS Sequence. Similar to STEAM, the 90° excitation pulse along with the two 180° refocusing pulses applied on the three orthogonal planes define a volume of interest (voxel) from which the signal is acquired.

The biggest disadvantage of MRS is that the entire signal within the defined voxel is summed and only one voxel is acquired leaving out any spatial information. Hence, prior knowledge of the location of the spectroscopic target is needed to decide the location of the single voxel.

2.2.3 Spectroscopic Imaging (SI):

As in MRI, spatial encoding would transform the single-voxel MRS to multi-voxel MRS imaging (MRSI).

The signal equation ignoring chemical shift is given as (see *Appendix I* for details):

$$S(t) = \int_x \int_y M(x,y) e^{-i(k_x(t)x + k_y(t)y)} dydx \qquad (2\text{-}5)$$

However, chemical shift would act as an additional dimension that needs to be properly sampled and included in the signal equation. Accordingly, Eq. 2-5 becomes [1]:

$$S(t) = \int_f \int_x \int_y M(x,y,f) e^{-i(k_x(t)x + k_y(t)y + 2\pi k_f f)} dydxdf \qquad (2\text{-}6)$$

where $k_x(t) = \gamma \int_0^t G_x d\tau$, $k_y(t) = \gamma \int_0^t G_y d\tau$ and $k_f = t$.

Hence, to fill the spatial-frequency space (k-space) we need to fill k_x, k_y and k_f. After acquisition, a 2-D Fourier transform is performed to reconstruct the signal from k-space to xy-space and a 3rd Fourier transform is then applied to transform the acquired signal at each voxel from time domain to frequency (chemical shift) domain.

To measure the nuclei's natural precession frequencies, i.e. chemical shift, no readout gradient is applied in the frequency encoding direction. Instead, both x and y directions are phase encoded.

2-D phase encoding can be incorporated to any MRS sequence hence transforming the single voxel sequence to an SI one. The most popular sequence, 2-D PRESS, is shown in Fig. 2-3. The main shortcoming of 2-D phase encoding is the very long scan times. For a 24×24 voxel scans, we have to step through k-space one step per repetition time (TR), resulting in 576 repetitions. Therefore, for a 1500 ms TR, a 24×24 voxel scan would take approximately 14 minutes.

Furthermore, phase encoding can be applied in the z-direction to perform multi-slice MRSI.[6] In that case, an additional Fourier transform is needed to reconstruct the voxels.

In addition to the previously mentioned MRSI techniques the 2-D phase encodes can be applied directly after the initial excitation pulse. This technique will be discussed in further detail in the next chapter.

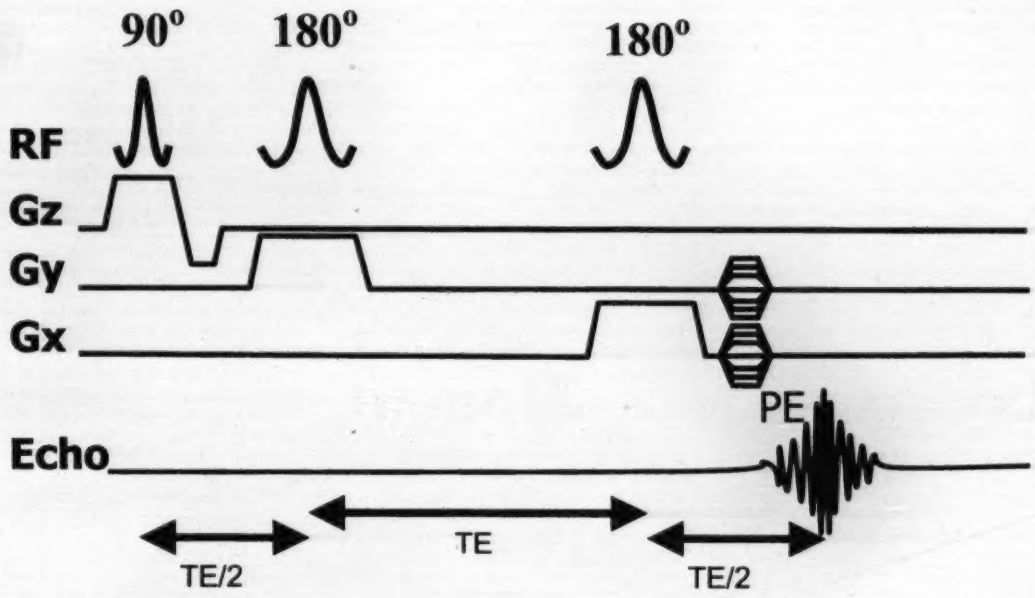

Figure (2-3): A schematic of a 2-D PRESS sequence

2.3 Signal and Noise Considerations:

In MRSI, the signal-to-noise ratio (SNR) is a very important factor that determines the quality of the spectra acquired in the scans. The need to maximize the SNR while maintaining achievable imaging parameters is crucial for *in-vivo* scans where noise levels are usually higher than *in-vitro* experiments. This section discusses the dependence of the signal and noise on the imaging parameters and hardware. Further SNR experiments are discussed in Chapter Three.

2.3.1 Signal:

The magnitude of the signal is proportional to 4 parameters:

1. Larmour frequency of the protons in the main magnetic field. EMF induced in the receiving coil is proportional to the rate of change of the magnetic flux Φ_B which in turn is proportional to the Larmour frequency ω_0.
2. The available magnetization vector M_0 which is dependent on:
    a. The energy difference between the spin-down and spin-up eigenstates. Where the relative populations of the spins in the spin-down / spin-up eigenstates at thermal equilibrium is:

    $$N_{\downarrow} / N_{\uparrow} = e^{-\mu B_0 / kT} \qquad (2\text{-}7)$$

    where $N_{\downarrow}$ and $N_{\uparrow}$ are the populations of the spins in the spin-down and spin-up eigenstates respectively (for details see *Appendix I* Eq. A-6 – Eq. A-8).

    b. The density of the spins in the sample

3. The amount of transverse magnetic field $\boldsymbol{B_T}$ that can be generated by the receiving coil. By reciprocity, this corresponds to the reception quality of the coil which defines the ability of the coil to convert the change in magnetic flux to electromagnetic force.
4. The spin response to the imaging sequence and parameters. For instance, repetition time (TR), echo time (TE), and flip angle.

Ignoring the fourth parameter and assuming constant spin density, the signal S is then:

$$S \propto \omega_0 M_0 V B_T \tag{2-8}$$

where V is the voxel volume. M_0 and ω_0 are both proportional to B_0, accordingly [1, 7]:

$$S \propto B_0^2 V B_T \tag{2-9}$$

2.3.2 Noise:

The main source of noise in magnetic resonance is thermal noise resulting from the Brownian motion of electrons which in turn generates random magnetic fields. Thermal noise arises mainly from the resistance in the receiving coil and the resistance of the imaged body as observed by the coil.

For thermal noise, the variance of the noise area of the signal can therefore be described as [1]:

$$\sigma_n^2 = 4k\,T\,R\,BW \tag{2-10}$$

where k is Boltzman's constant, T is the temperature in Kelvin, and R is the total resistance of the coil (R_c) and the imaged body (R_b). BW is the bandwidth of the signal which is equal to sampling bandwidth.

Thermal noise is Gaussian distributed, white, and additive; hence, noise is the square root the variance. From Eq. 2-10:

$$Noise = \sqrt{\sigma_n^2} \propto \sqrt{R} \tag{2-11}$$

and,

$$R = R_c + R_b \tag{2-12}$$

From Eq. 2-11 and Eq. 2-12:

$$Noise \propto \sqrt{R_c + R_b} \tag{2-13}$$

where R_c and R_b are proportional to $\omega_0^{1/2}$ and ω_0^2 respectively [1].

However, resistance in MRI is generally dominated by the resistance of the imaged body rather than the coil, hence Eq. 2-13 becomes [1]:

$$Noise \propto \sqrt{R_b} \propto \omega_0 \propto B_0 \tag{2-14}$$

Another factor affecting noise is the number of phase encodes. Due to the Fourier transforms applied to reconstruct the images, noise is averaged out. If k-space consists of N points in one direction, after the Fourier transform the noise is proportional to $(1/N)^{1/2}$.[1, 7] Accordingly, for phase encoding steps equal to N_P [1, 7]:

$$Noise \propto \frac{1}{(N_P)^{1/2}} \tag{2-15}$$

For MRSI, where phase is used to encode both the x and y directions:

$$Noise \propto \frac{1}{(N_{P_x} N_{P_y})^{1/2}} \tag{2-16}$$

Overall noise is then:

$$Noise \propto B_0 (\frac{1}{N_{P_x} N_{P_y}})^{1/2} \tag{2-17}$$

2.3.3 Signal-to-Noise Ratio (SNR):

Recall Eq. 2-10 [1]:

$$\sigma_n^2 \propto BW_{sam} \tag{2-18}$$

where BW_{sam} is the readout sampling bandwidth and is defined as:

$$BW_{sam} = Number\ of\ samples / readout\ time\ (T_{readout}) \tag{2-19}$$

While the signal is independent of BW_{sam}, doubling the readout time ($T_{readout}$) halves BW_{sam} which in turn decreases the noise by $\sqrt{2}$ as shown in Eq. 2-20.

$$Noise = \sqrt{\sigma_n^2} \propto \sqrt{\frac{BW_{sam}}{2}} \tag{2-20}$$

Comparing SNR_1 to SNR_2 with readout times equal to $T_{readout}$ and $2\times T_{readout}$ respectively:

$$SNR_2 / SNR_1 \propto \frac{S}{\sqrt{\frac{BW_{sam}}{2}}} \times \frac{\sqrt{BW_{sam}}}{S} = \sqrt{2} \qquad (2\text{-}21)$$

Generally, the SNR is related to the readout time ($T_{readout}$) such that [1]:

$$SNR \propto \sqrt{T_{readout}} \qquad (2\text{-}22)$$

Therefore from Eq. (2-9), Eq. (2-17) and Eq. (2-22):

$$SNR \propto \frac{S\sqrt{T_{readout}}}{Noise} \propto \frac{B_0{}^2 V B_T \sqrt{T_{readout}}}{B_0 (\frac{1}{N_{P_x} N_{P_y}})^{1/2}} \propto B_0 V B_T (N_{P_x} N_{P_y} T_{readout})^{1/2} \qquad (2\text{-}23)$$

Therefore, in MRSI it is desirable to use high B_0 field strengths and long readout times. Also, in high-resolution MRSI, high B_0 field strengths help offset the decrease in SNR that occurs to the decrease in voxel size

References:

1. Nishimura, D.G., *Principles of Magnetic Resonance Imaging*. 1996: Stanford University.
2. Frahm, J., Bruhn, H., Gyngell, M.L., Merboldt, K.D., Hanicke, W., Sauter, R., *Localized proton NMR spectroscopy in different regions of the human brain in vivo. Relaxation times and concentrations of cerebral metabolites.* Magn. Reson. Med., 1989. **11**(1): p. 47-63.
3. Bottomly, P.A., *Selective volume method for performing localized NMR spectroscopy*, U. Patent, Editor. 1984.

4. Gordon, R.E., Ordidge, R.J. *Volume selection for high resolution NMR studies.* in *Abstracts of the Society of Magnetic Resonance in Medicine 3rd Annual Meeting.* 1984. New York.
5. Ordidge, R.J., Bendall, M.R., Gordon, R.E., Connelly, A., *Magnetic Resonance in Biology and Medicine*, ed. G.Govil, C.L. Khetraplal, and A. Saran. 1985, New Delhi: McGraw-Hill. 387-397.
6. Li, X., Jin, H., Lu, Y., Oh, J., Chang, S., Nelson, S.J., *Identification of MRI and 1H MRSI parameters that may predict survival for patients with malignant gliomas* NMR Biomed. , 2004. **17**(1): p. 10-20.
7. Haacke, E.M., *Magnetic Resonance Imaging, physics principles and sequence design.* 1999: John Willey & Sons.

Chapter Three

3 Assessment of Biological Tumor Delineation Using a Gel Phantom

3.1 Introduction:

Excellent soft tissue contrast of Magnetic Resonance Imaging (MRI) has made it a valuable tool in the diagnosis and the treatment planning of cancer. Due to its long scan times and low signal-to-noise, Magnetic Resonance Spectroscopic Imaging (MRSI) has never achieved the broad utility of its imaging cousin. However, with technological advancements in the form of higher field strengths, stronger gradients, and novel pulse sequences, biochemical imaging in the form of MRSI is becoming more practical and effective in the diagnosis and assessment of cancer.[1, 2]

The advantages that spectroscopic imaging can offer cancer therapy are significant. By measuring different metabolite levels - effectively a means of non-invasive biopsy - MRSI can detect tissue abnormalities that may not yet be visible in conventional MRI. Pirzkall et al. and Pallud et al. have shown that tumor extent as shown by MRSI may differ greatly from the extent shown on conventional MRI scans.[3, 4] Moreover, Walecki et al. have shown that MRSI may help in identifying patients who have a high risk of recurrence.[5] This has led to an increase in interest in incorporating MRSI into treatment planning by adding a biological target volume in the contouring process. More recently, several methods of tumor identification and

registration techniques have been used to integrate MRSI results into the radiotherapy process.[6, 7] Such studies have demonstrated that the delineation of the tumor volume in treatment plans for radiotherapy has changed when MRSI metabolite information was considered.[7] Initial results showed that MRSI can detect regions of abnormal activity (tumor) that would not have been covered using conventional imaging and contouring methods.

However, one of the major drawbacks of MRSI has always been its poor spatial resolution. Reported nominal voxel sizes have typically been on the order of 1 cm^3 ($8\times8\times10$ mm^3 - $10\times10\times10$ mm^3). [8] This low resolution may lead to metabolite maps suffering from partial volume averaging. If MRSI is to be used in conjunction with images for treatment planning purposes, it is very important that the effect of voxel size on the accuracy of the spatial metabolite maps be investigated.

The aim of this chapter is to investigate the effect of reduced voxel sizes on the SNR and the measured metabolite ratios at 3 T. The nominal voxel sizes investigated ranged from $5\times5\times10$ mm^3 to $6.67\times6.67\times10$ mm^3. Also, we are introducing a phantom-based method to quantitatively compare the differences between high-resolution and low-resolution MRSI in accurately detecting the geometry of a solid tumor.

3.2 Materials and Methods:

In the work that follows, a 3 Tesla MR system is utilized to generate high-resolution MRSI metabolite maps with voxels ranging from 0.25 cm^3 (5×5×10 mm^3) to 0.44 cm^3 (6.67×6.67×10 mm^3) in nominal size. As illustrated in Chapter Two, 3 T MRI has the advantages of improved signal-to-noise ratio (SNR) and larger chemical shifts over conventional 1.5 T units which helps compensate for the inherent decrease in SNR when using such small voxels.[9]

Chemical shift is expressed as:

$$\omega = \gamma B_0(1-\sigma) \tag{3-1}$$

where B_0 is the main static magnetic field and σ is the shielding constant, which is unique to the local environment of the nucleus.

As shown in Eq. 2-23, SNR is related to B_0 as:

$$SNR \propto B_0 \tag{3-2}$$

It is however important to mention that experimental measurements show that in some instances the increase in SNR is not necessarily linear with respect to B_0.[10]

Firstly, the parameters for a Spin Echo Spectroscopic Imaging (SESI) sequence were adjusted so that MRSI datasets covering most of the brain could be

produced in a clinically acceptable time.[11] Next, measurements were done *in-vitro* to assess the effects of decreasing the voxel size on the spectral SNR and the metabolite ratios used for tumor delineation. Finally, a specialized gelatin phantom was constructed with sharply defined physiological metabolite distributions. This phantom was scanned both with high-resolution and low-resolution MRSI sequences to evaluate the magnitude of delineation errors that can result from the use of conventional low-resolution scans.

All phantom and volunteer studies (ETH 21780, Cross Cancer Institute, Multimodality functional imaging (MRSI and dynamic contrast enhancement MRI) predicts tumor migration, invasiveness, and patterns of failure of human Glioblastoma treated with concurrent radiation therapy and Temozolomide, Principal Investigator: B. Abdulkarim) were conducted on a Philips Intera 3 T MRI (Philips Medical Systems, Bothell, WA) unit together with a transmit/receive birdcage head coil. Volunteer exams consist of two scan types: a series of anatomic scans for the anatomic identification of the volume of interest, followed by the spectroscopic imaging scan.

The primary brain metabolites considered in this work are choline (Cho), creatine (Cr), and N-acetylaspartate (NAA). Choline reflects membrane synthesis and turnover and typically increases in tumors.[2] Creatine reflects the energetic status of tissue. It is typically considered to remain constant in tumors and normal tissue, however, in some cases Cr was shown to decrease in brain tumors.[2] NAA

decreases in brain tumors possibly due to a decrease in the density or function of neuronal cells.[12-16] Cancerous tissue can be differentiated from healthy tissue through a calculation of the ratio of Cho/NAA.[2]

3.2.1 Spectroscopic Imaging Scan:

There are multiple ways to perform spectroscopic imaging. One of the most popular sequences is the two-dimensional point resolved spectroscopy (2-D PRESS), which acquires signal only from a predefined volume commonly known as the PRESS box.[17-19] In 2-D PRESS, two phase encodes are applied to divide the PRESS box into voxels. This sequence can be extended to a three dimensional sequence by utilizing three phase encodes.[1] The 3-D PRESS technique is effective in selectively exciting a volume-of-interest (VOI), and would allow for scanning sub-anatomic MRSI fields-of-view (FOV) without any fold-over artifacts. However, 3-D PRESS requires relatively long scan times, and for this reason it was not utilized in this work.

In our studies, a Spin Echo Spectroscopic Imaging (SESI) technique was used to generate metabolite maps.[11] This technique is based on the generation of signal from the entire slice by means of a spin echo, rather than using PRESS to excite a specific region. Two phase encodes are incorporated into the sequence to encode the signal into a specified field of view (Fig. 3-1).

SESI has the advantage of faster scan times because it can be combined with Turbo Spectroscopic Imaging (TSI). TSI allows for multiple phase encodes to be collected over the same repetition time (TR).* It works by repeating the last echo pulse and gradients, which leads to the generation of a train of echoes. Each of these echoes is phase encoded and acquired separately.[20] The turbo factor refers to the number of echoes present in each train (Fig. 3-1).

There are a number of disadvantages to using TSI. Firstly, the centre of k-space is filled with the signal from the first echoes while is the edges are filled with the subsequent echoes. Accordingly, the sequence is more susceptible to T2 weighting artifacts that can manifest themselves in the form of blurring or enlarged effective voxel sizes. During the time separating the echoes, the signal suffers from T2 decay. Increasing the turbo factor increases the time between the first and last echoes, thus, increasing the T2 decay. The increase in T2 decay results in increasing the T2 weighting artifacts mentioned above. Accordingly, to reduce the total scan time while minimizing the T2 weighting artifacts the turbo factor was set to 2.

Another disadvantage of our technique is the shorter readout times (128 ms) associated with TSI compared to the long readout times (~500 ms) typical of PRESS and STEAM techniques. While this directly leads to a decrease in SNR, a later

* Philips Medical Systems Nederland B.V., New Intera Release 10.4 Application Guide volume 4, 2004.

discussion will show that our technique still yields an acceptable SNR for metabolite peak detection and analysis.

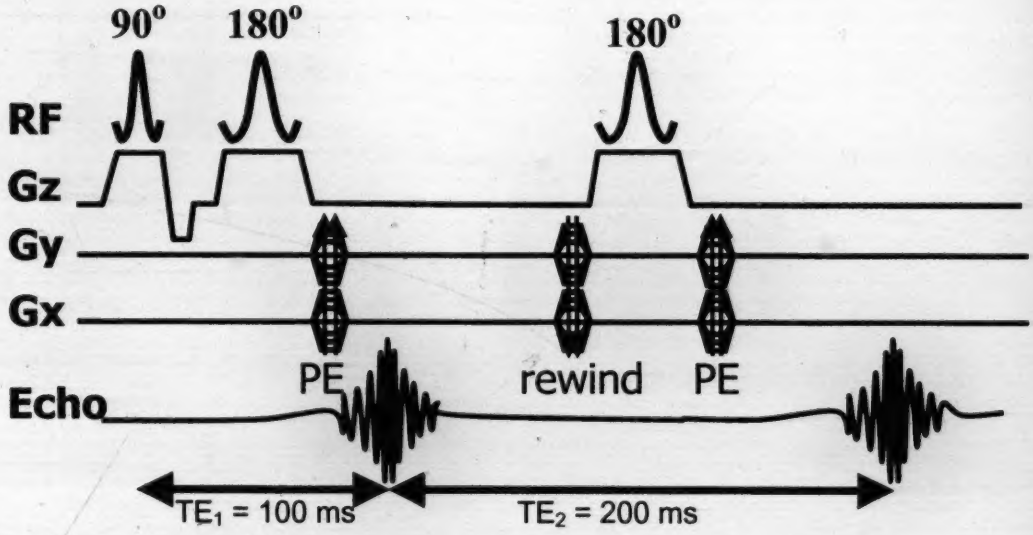

Figure (3-1): A schematic of an SESI sequence with TSI turbo factor of 2. TE_1 and TE_2 are the first and second echo times respectively.

We used the SESI sequence with TSI because it can provide improved coverage of the brain with high resolutions compared to a typical 3-D PRESS. A 6-slice SESI sequence with TSI takes about 17 minutes for a high-resolution scan, which is comparable to the scanning time of low-resolution 3-D PRESS sequences.[4] The following sub-sections discuss some of the common terms and parameters related our MRSI scanning technique.

3.2.1.1 Nominal Spatial Resolution:

Nominal voxel sizes in MRSI are expressed as:[11]

$$\begin{aligned} \Delta z &= 2\pi BW_{rf} / \gamma G_z \\ \Delta x &= FOV_x / N_{P_x} \\ \Delta y &= FOV_y / N_{P_y} \end{aligned} \qquad (3\text{-}3)$$

where, Δx and Δy are the nominal voxel sizes in the transverse plane and Δz is the nominal transverse slice thickness. BW_{rf} is the bandwidth of the slice-selection pulse, γ is the gyromagnetic ratio equal to 6.796 radians/(second · Tesla), and G_z is the slice-selection gradient. N_{Px} and N_{Py} are the number of phase encodes in the x and y directions respectively.

Therefore, the in-plane resolution can be improved by either increasing the number of phase encodes or decreasing the field of view of the scan. However, from Eq. 2-23:

$$SNR \propto B_0 V B_T (N_{P_x} N_{P_y} T_{readout})^{1/2} \qquad (3\text{-}4)$$

SNR is dependent on the both the voxel size and the number of phase encodes. Thus, to correctly investigate the effect of voxel size on the SNR, the voxel size was varied only by changing the FOV and using the same number of phase encodes in both the high- and low-resolution scans.

3.2.1.2 Effective Voxel Size:

In order to reduce noise a 2-D cosine filter was multiplied by k-space. The profile of the filter (W) in one direction is shown in Eq. 3-5:

$$W = \cos\left(\frac{\pi}{2} \times \left[\frac{x + \frac{1}{2}}{\frac{N_p}{2}} - 1\right]\right) \qquad (3\text{-}5)$$

where N_p is the number of phase encodes in one direction, and $0 \leq x \leq N_p\text{-}1$

The application of the filter leads to reducing the amplitude of high spatial-frequencies which translates into reduced spatial resolution. Post-filtering, the effective voxel size is on the order of 1.5 times larger than the quoted nominal voxel size.

3.2.1.3 Field of View (FOV):

High-resolution scans are based on setting the FOV between 120×120 mm^2 – 160×160 mm^2 minimizing the FOV as much as possible while paying attention to possible aliasing regions.

3.2.1.4 Volume of Interest (VOI):

The volume-of-interest (VOI) is the volume from which the best signal is desired. It was chosen to be about 95×95×60 mm^3 covering most of the brain or a region-of-interest (ROI) in phantoms.

3.2.1.5 Shimming:

Shimming is a term used to describe the process of improving the homogeneity of the static magnetic field B_0. Inhomogeneities in the static magnetic field B_0 would influence the precession frequency (chemical shift) $\omega$of the metabolites being investigated as shown by Eq. 3-6.

$$\omega = \gamma B_0(1-\sigma) \tag{3-6}$$

where $\sigma$is the shielding constant for the molecule in question.

In the shimming process, an MR pulse sequence is used to measure the various orders of magnetic field gradients (inhomogeneities) present in the imaging subject (VOI). Magnetic field inhomgenieties can be estimated as:

$$\begin{aligned} inhomogenieties = {} & a_1x + a_2y + a_3z + a_4x^2 + a_5y^2 \\ & + a_6z^2 + a_7xy + a_8xz + a_9zy \end{aligned} \tag{3-7}$$

where a_1-a_9 are constants while x, y and z are variables along the x, y , and z directions respectively.

As shown in Eq. 3-7, magnetic field inhomogeneities can be estimated by a combination of first-order and second order gradients. In the first order components (x. y. z), the magnetic field varies linearly with respect to position in the magnet. In second order components (x^2, y^2, z^2, *xz, xy, and zy)*, the magnetic field varies in a

quadratic fashion with respect to position. A special set of shim and gradient coils are utilized to correct for magnetic field inhomogeneities.

Shim and gradient coils are designed to generate first- and second-order magnetic field gradients similar to Eq. 3-7. Those gradients are applied in a manner so that first-order (linear) or second-order (quadratic) inhomogeneities in the static field B_0 are corrected. In first-order shimming, shim and gradients coils are applied to compensate for the linear components of the inhomogeneities (x, y, and z) shown in Eq. 3-7. In second-order shimming, the coils are applied to compensate for the quadratic components of the inhomogeneities (x^2, y^2, z^2, xz, xy, *and* zy) shown in Eq. 3-7, in addition to first-order corrections.

Magnetic field gradient corrections can therefore be expressed as:

$$\begin{aligned} \textit{gradient corrections} = & -a_1 x - a_2 y - a_3 z - a_4 x^2 - a_5 y^2 \\ & - a_6 z^2 - a_7 xy - a_8 xz - a_9 zy \end{aligned} \tag{3-8}$$

where a1-a9 are the constants estimated in Eq. 3-7.

In our work second-order shimming is performed to improve the homogeneity of the static magnetic field B_0 over the VOI. As shown in Eq. 3-8, the first- and second-order components of the magnetic field inhomogeneities are corrected by magnetic field gradients produced by shim and gradient coils.

3.2.1.6 Aliasing (fold-over) artifacts:

Aliasing is caused by inadequate sampling of k-space which translates into inadequate coverage of the imaged body by the FOV in the imaging-space. Due to the excitation of the whole slice, aliasing artifacts will occur when the reconstruction FOV is smaller than anatomy within the slice. In phase encoding, spins are encoded with phases spanning from $-\pi$ to π. Spins with phases of $-\pi/2$ and $+3\pi/2$ will be mapped to the same position corresponding to $-\pi/2$. Accordingly, a point lying outside the FOV will be phase encoded and incorrectly mapped to the opposite side of image, hence the name fold-over. Since, in our case, high resolutions are achieved by reducing the FOV, there is greater potential for the presence of aliasing artifacts in our scans.

To reduce fold-over artifacts, a series of radio-frequency (RF) pulses and crusher gradients were applied to suppress the unwanted signal outside the VOI and FOV. Signal suppression is applied prior to the application of the imaging sequence shown in Fig. 3-1. An excitation RF pulse is applied to selectively excite an unwanted slab of spins outside the VOI. Strong gradients known as crusher gradients are applied causing the dephasing of the spins. This dephasing leads to the loss of coherence of the spins and ultimately complete signal loss. After suppression, the imaging sequence (Fig. 3-1) is applied where the acquired signal contains minimum contributions from the suppressed spins. In our scans, ten sets of those RF pulses and crusher gradients were applied surrounding the VOI to reduce fold-over.

Moreover, the FOV was usually chosen with the intent of preventing any aliasing artifacts, regardless of crusher gradients, from interfering with the VOI.

3.2.1.7 Water Suppression:

Due to the abundance of water its signal can sometimes mask the signal from some metabolites. Accordingly, the water signal has to be suppressed to better visualize the peaks of the metabolites of interest. Water suppression is achieved by applying a chemical shift selective (CHESS) excitation pulse for water and then applying crusher gradients.[21, 22] This yields a dephased negative water peak that tends to return to equilibrium through T_1 relaxation. CHESS suppression is further combined with an inversion recovery technique by starting the measurement at the zero crossing of the water peak. Furthermore, after k-space reconstruction, a Digital Shift Accumulation (DSA) filter is applied on the time domain data giving a secondary stage of water suppression in the preprocessing phase.* The DSA filter works by shifting the time-domain signal and subtracting this from the original signal. The signal with zero chemical shift (water frequency) will be nulled. The number of points by which the filter is shifted determines an optimum frequency which is not attenuated by the filter. For our work the shift was adjusted to place optimum frequency close to that of NAA.

---

* Philips Medical Systems Nederland B.V., New Intera Release 10.4 Application Guide volume 4, 2004.

3.2.2 Processing:

The raw acquired data from the MRSI scans were reconstructed from k-space and preprocessed on the console, generating a spectrum for each spatial location in the imaging grid. The data was exported to Matlab where it was further analyzed using in-house developed software that calculates the area under different metabolite peaks.

The software evolved over the duration of the project. The first attempts of peak area calculations depended on user defined integration boundaries. Peak integration was calculated as the sum of the points lying between the integration boundaries on the modulus spectrum. Although this method is routinely used for rough estimations of peak strengths it suffered from serious flaws.[23] Firstly, the boundary definition method was user dependant which inherently introduces user bias. Secondly, the use of modulus data for peak integration was not accurate because noise on the modulus spectrum is always positive which introduces baseline artifacts. Alternatively, a peak fitting algorithm was developed to calculate peak heights and areas more accurately.

Peak fitting relies on the basic assumption that the free induction decay (FID) (time-domain) signal acquired in spectroscopy is a sum of exponentially decaying sinusoids. Accordingly, in the frequency domain the spectrum would consist of a sum of Lorentzian lines.[23] The developed peak fitting algorithm fits a sum of Lorentzians to the complex spectra based on seeding values for the peak locations,

estimated peak heights and full width half maxima (FWHM).[23] The equation for the real Lorentzian used in peak fitting is given by:

$$L_{real} = \frac{a^2 I}{a^2 + 4(x - x_0)^2}\cos(\phi) + \frac{2aI(x - x_0)}{a^2 + 4(x - x_0)^2}\sin(\phi) \qquad (3\text{-}9)$$

Where a is the FWHM, I is the height of the peak at zero phase, ϕ is the phase angle, and x_0 is the peak location.

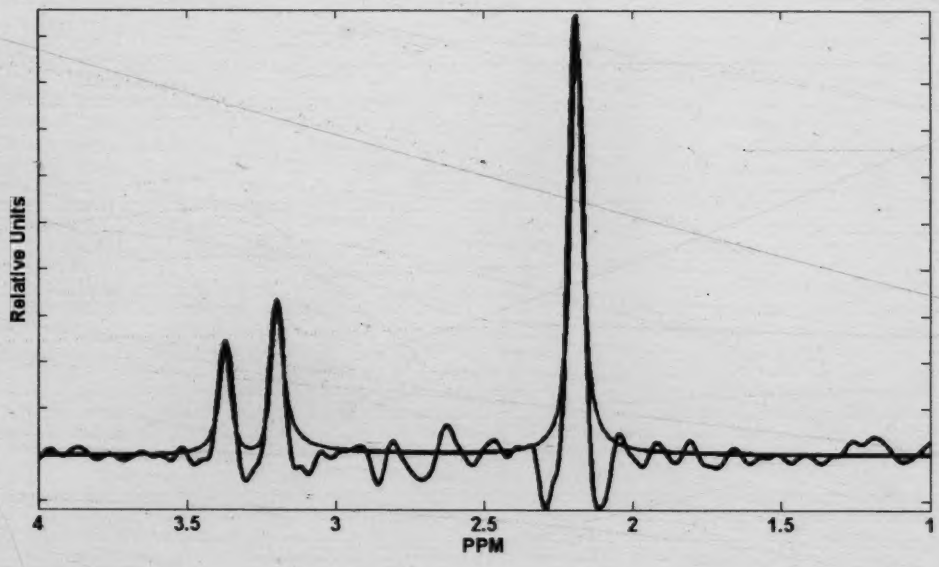

Figure (3-2): A typical spectrum showing the NAA, Cho, and Cr peak. The blue line represents the raw spectrum while the red line represents the fitted spectrum. The under shooting in the raw spectrum at approx. 2.1 and 2.3 ppm is caused by noise and ringing artifacts.

The software uses a least squares algorithm that estimates the parameters that would minimize Eq. 3-9 over the fitting region. An example of the results is shown

in Fig. 3-2 where the correlation coefficient over the fitting region was found to be 96.6%. (See *Appendix II* for details on the algorithm)

$$F_{sum} = \sum_{m}^{N-1} (F_{raw} - F_{fit})^2 \qquad (3\text{-}10)$$

where, F_{raw} and F_{fit} are the raw and fitted spectrum respectively.

The goodness-of-fit (Chi-squared (χ^2)) parameter was calculated for the three metabolite peaks as:

$$\chi^2 = \sum_{i} \frac{(O_i - E_i)^2}{E_i} \qquad (3\text{-}11)$$

where, i is the number of bins, O_i is the observed frequency of bin i and E_i is the expected frequency of bin i.

For 95% confidence, the calculated χ^2 has to be less than of equal to a critical $\chi^2_{critical}$. For Cho, Cr and Naa χ^2 was found to be 10.58, 1.68 and 3.17 respectively. Those results were all less than $\chi^2_{critical}$ of 11.07, 11.07 and 14.067 for Cho, Cr, and NAA respectively. Therefore, the goodness-of-fit was acceptable.

The Lorentzian parameters (peak heights, locations, FWHM, and phases) resulting from the peak fitting algorithm are used in the software to analytically calculate the area under the peaks from each real spectrum using Eq. 3-12.

$$L_{area} = \frac{1}{2}\pi a l \qquad (3\text{-}12)$$

Finally, the software produces metabolite maps for choline, creatine, and NAA, as well as a ratio map of Cho/NAA.

Interpolation of the metabolite maps has been routinely used in the literature to correlate MRSI with CT and MRI images for treatment planning.[2] The interpolation results in smoothing the metabolite maps and allows for better comparison with CT and MRI images. In this work, the metabolite maps were interpolated to 256×256 voxels (approx. 0.47×0.47×10 mm^3/voxel).

Interpolation can be performed using two methods: 1. Pre-processing zero-filling interpolation of the *k-space* data; 2. Post-processing interpolation of the metabolite maps. Using *k-space* pre-processing interpolation is considered more accurate since it involves the interpolation of the spectra themselves, however, it would increase the number of voxels to be processed by two orders of magnitude. Accordingly, linear interpolation of the metabolite maps was chosen to reduce the processing time. Post-processing interpolation provides visually smoother metabolite maps, however, this is not a result of the interpolation for the spectra themselves and hence are regarded as less accurate than pre-processing interpolation. The error in the interpolation between the two methods can be estimated through either simulation or phantom measurements. This is however beyond the scope of interest of this work.

3.2.3 Phantom Studies:

A phantom was constructed using a cuboid (9 cm x 9 cm x 15 cm) plastic container filled with uniform concentrations of metabolites. Approximately 4 mM choline chloride and 10 mM creatine hydrate were used to reflect physiological levels in a healthy brain.[10] Choline and creatine were chosen for this phantom for two reasons. Firstly, because choline and creatine are of lower concentration and signal than NAA in a normal brain, they would be more sensitive to changes in SNR. Secondly, the close spectral proximity of the primary peaks of choline (3.2 ppm), and creatine (3.0 ppm) makes the scans more sensitive to spectral blurring. This phantom was used to perform the *in-vitro* spectral SNR study and to investigate the effects of voxel size on metabolite ratios.

3.2.3.1 Spectral SNR study:

The phantom was scanned using a single slice TSI scan with TR of 1500 ms. Four spatial nominal resolutions were used (10×10×10 mm^3/voxel, 5×5×10 mm^3/voxel, 4.17×4.17×10 mm^3/voxel, and 3.33×3.33×10 mm^3/voxel). The spectra were then analyzed and the spectral SNR was defined and calculated as the area of the Cr peak divided by the root-mean-square (RMS) of the noise. The noise window was centered at -4.5 ppm with width of 1 ppm (Fig. 3-3).

$$SNR = \frac{area(Cr)}{RMS(noise)} \qquad (3\text{-}13)$$

The SNR was calculated and averaged over a uniform ROI (Fig. 3-4). It is expected that the spectral SNR would decrease as the voxel size decreases. For more insight into the signal and noise analysis in the MRSI please refer to *section 2.3.*

For *in-vivo* studies, the SNR was calculated and averaged over an ROI at both high and low resolutions ($5.83\times5.83\times10$ mm^3 and $9.58\times9.58\times10$ mm^3 nominal voxels, respectively). The volunteer scans were acquired with a TR of 1500 ms. Another volunteer scan was acquired at 4 slices with TR 5500 ms with nominal voxel sizes of $5\times5\times10$ mm^3. Sampling bandwidth for all SNR studies was kept at 2700 Hz.

To establish a standard to assess whether the resulting SNRs were acceptable, the means and standard deviations of the creatine peak and noise heights were calculated over the same ROI (Fig. 3-4). Statistically the means of the noise and creatine peak heights should be separated by at least 1.97 standard deviations to achieve 95% confidence that the two distributions are not related. Hence, acceptable SNR was taken to correspond to the scan where the mean height of the creatine peak is at least 2 standard deviations higher than the mean noise level. This criterion guarantees that the user and the fitting algorithm would be able to clearly distinguish between the metabolite peaks and the noise.

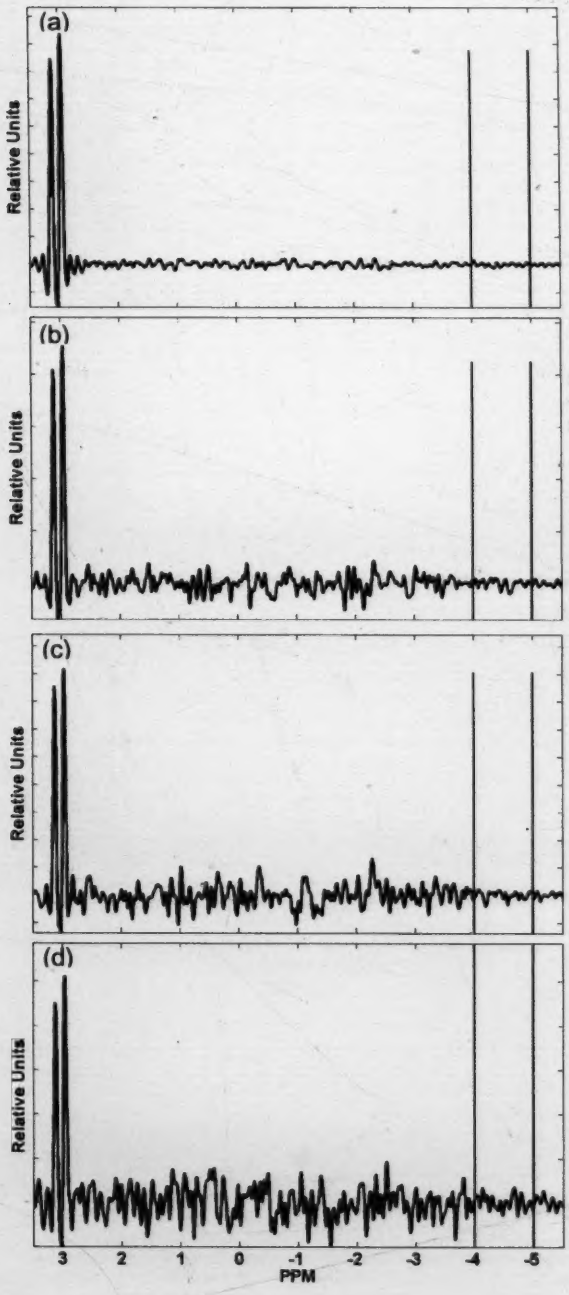

Figure (3-3): Typical Spectra individually scaled from SNR study. (a) 10×10×10 mm^3/voxel scan, (b) 5×5×10 mm^3/voxel scan, (c) 4.25×4.24×10 mm^3/voxel scan ,and (d) 3.33×3.33×10 mm^3/voxel scan. The displayed window is the noise window.

3.2.3.2 Effects of Voxel Size on Metabolite Ratios:

Utilizing the same uniform phantom and scans described in the *in-vitro* spectral SNR study, the areas under the choline and creatine peaks were calculated from the results of the peak fitting algorithm.[23] The Cho/Cr ratio was then calculated and averaged over a homogeneous region in the phantom (Fig. 3-4). This procedure was intended to test whether the mean value of the ratios would remain the same over the different scan resolutions.

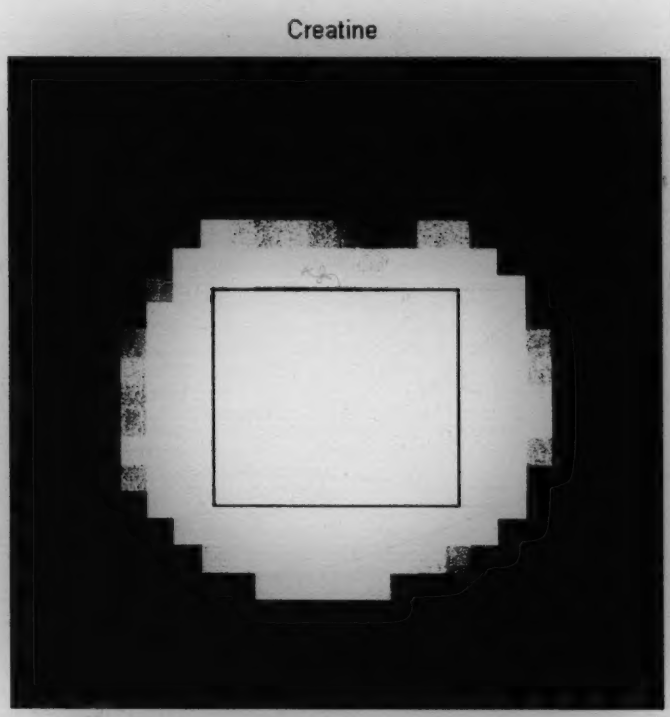

Figure (3-4): Creatine metabolite map of the uniform phantom showing the ROI used for the SNR and metabolite ratio studies.

3.2.4 Comparison of High-Resolution with Low-Resolution MRSI:

Currently, most available phantoms are designed for single voxel spectroscopy. Phantoms utilizing acrylic or glass containers are likely to suffer from susceptibility artifacts arising from the interface of the wall material and the solution used to fill the phantom. Those artifacts are more pronounced in high-detail and irregularly shaped phantoms. Moreover, acrylic or glass walls have a finite thickness which may lead to partial volume artifacts in the spectral data. The phantom developed in this work is made up of porcine gel which negates the need for an acrylic or glass container. This eliminates susceptibility and zero-averaging partial volume artifacts. There is however, the potential for the diffusion of metabolite across the phantom boundaries which might affect the accuracy of the results.

A phantom designed to simulate tumors was constructed using 5% by weight porcine gel containing clinically relevant concentrations of choline chloride (4 mM) and creatine hydrate (10 mM).[10]

A cast acrylic wedge (base: 3.8 cm × 3.8 cm, height: 9 cm) was inserted in the liquid gel and was later removed when the gel hardened. The void left by the wedge was filled with a solution containing elevated levels of choline chloride (10 mM), and the same concentration of creatine as in the background (Fig. 3-5). The increase in choline concentration inside the wedge-shaped void would simulate the presence of a malignancy.

It is worth mentioning that three methyl (CH_3) molecular groups contribute to the 3.2 ppm choline peak, whereas, only one contributes to the 3.0 ppm creatine peak. Therefore, even though the choline concentration maybe less than that of creatine, the choline peak can be of equal to or sometimes larger than the creatine peak.

The phantom was scanned 10 times at the same position with high-resolution and low-resolution scans of nominal voxel sizes 5×5×10 mm^3 and 10×10×10 mm^3, respectively. The shim settings and water suppression parameters were reset before each scan.

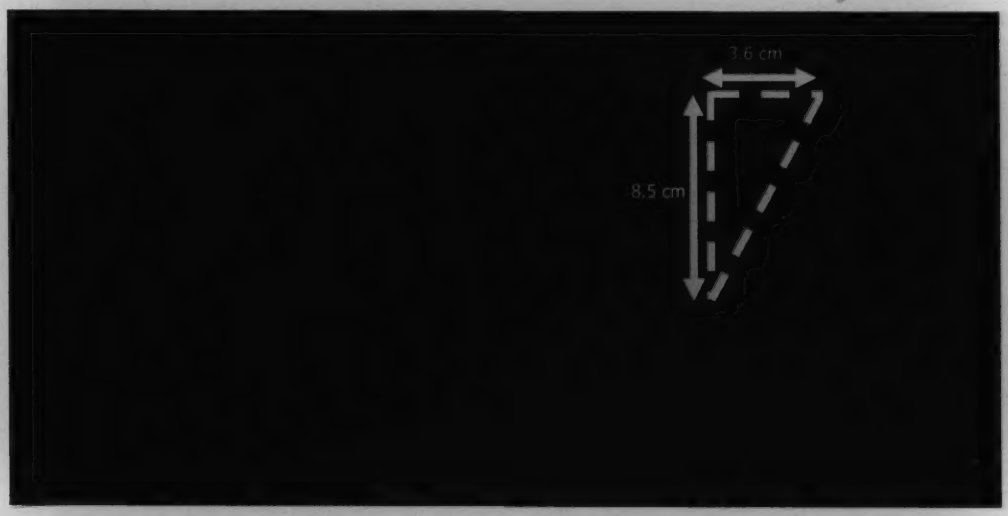

Figure (3-5): T2 weighted transverse image of the wedge phantom. The dashed lines outline the wedge. The dimensions shown are smaller than the ones quoted due to partial immersion of the wedge in the gel.

A single-slice anatomic scan of the phantom with $0.47\times0.47\times10$ mm^3 voxels was acquired at a position coinciding with the spectroscopic scan. This allowed a proper comparison of the spectroscopic results to the phantom geometry. The Cho/Cr ratio maps were calculated for 10 spectroscopic scans. Three binary masks were produced for Cho/Cr ratios $\geq$ 1.5, $\geq$1.75, and $\geq$ 2, respectively to show the spectroscopic representation of the wedge at different Cho/Cr ratios. (Fig. 3-6) A similar binary mask was produced from the anatomic scan to represent the actual geometry of the wedge shape. The binary masks of the spectroscopic scans were compared to the one corresponding to the anatomic scan by using Eq.(3-14):

$$result = (Cho/Cr)\,binary\,mask - 2\times Anatomic\,binary\,mask\,. \qquad (3\text{-}14)$$

This equation would then result in an image containing the following pixel values: 1 for anywhere the representation of the wedge by the spectroscopic scans is larger than that of the anatomic scan, -1 for the areas of agreement between the spectroscopic imaging and the anatomic scans, and -2 for the regions of the wedge on the anatomic scan that are not represented on the spectroscopic scan. It is expected that the high-resolution scans would show better definition in the extent and the shape of the wedge-shaped phantom.

Low Diffusion Phantoms

Two similiar phantoms with 5% and 15% by-weight gel concentrations were constructed in the same manner as the previous wedge phantom. The metabolite

concentrations in the gel were chosen to imitate those of normal tissue; 2.3 mM Cho, 10 mM Cr, and 15 mM NAA.[24, 25] The wedge was filled with a solution that imitated mimicking glioblastoma; 8 mM Cho, 3 mM Cr, and 5 mM NAA.[25, 26] To minimize the effect of diffusion on the validity of the results, scans were performed immediately after the introduction of the metabolite solution. In half of the studies, the low-resolution ($10\times10\times10$ mm^3/voxel) scan was performed first, and in the other half the high-resolution scans ($5\times5\times10$ mm^3/voxel) were performed first. In this way, valid comparisons could be drawn between the different resolutions over and above any effects of diffusion.

It is expected that if diffusion was not a factor affecting our phantom design that the all phantoms would qualitatively show the same pattern of difference between high and low resolution scans.

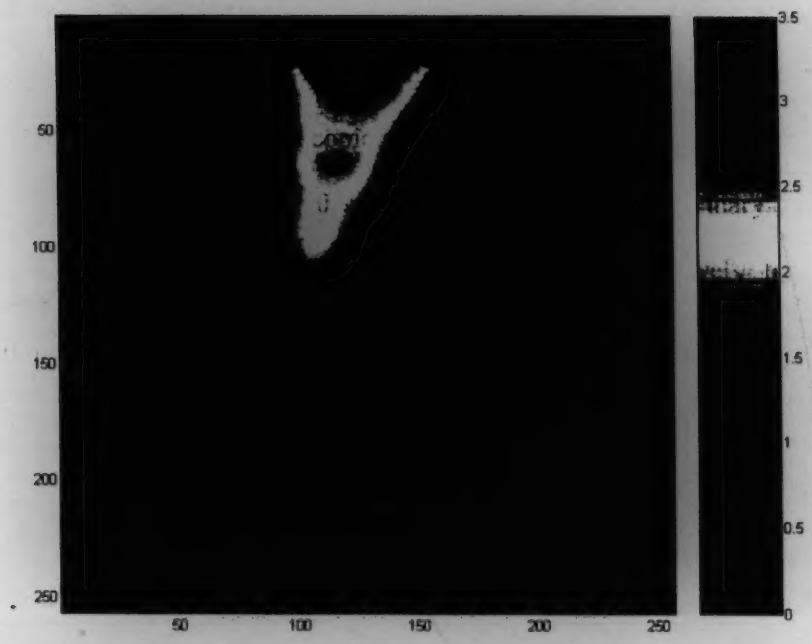

Figure (3-6): Cho/Cr ratio map of the phantom with a contour (black) at Cho/Cr = 1.75. The image is masked around the VOI.

3.2.5 Volunteers and Clinical Subject Studies:

Healthy volunteers and clinical subjects diagnosed with GBM were scanned after obtaining ethics approval (ETH 21780, Cross Cancer Institute, Multimodality functional imaging (MRSI and dynamic contrast enhancement MRI) predicts tumor migration, invasiveness, and patterns of failure of human Glioblastoma treated with concurrent radiation therapy and Temozolomide, Principal Investigator: B. Abdulkarim). The parameters for a six-slice scan were adjusted in order to minimize the total scan time while maintaining the full tumor coverage and achieving the highest spatial resolutions possible.

Scanning parameters were set as follows: TR of 3800 ms, TE_1 of 100 ms, TE_2 of 200 ms, spectral bandwidth of 4000 Hz, 512 point spectral sampling, 24×24 phase encoding matrix, six 10 mm thick slices and 0 mm gaps. This provided a nominal spatial resolution of 5×5×10 mm^3/voxel - 6.67×6.67×10 mm^3/voxel. The number of echoes acquired per repetition (turbo factor) was set to 2 in order to reduce T2 weighing artifacts associated with acquiring more than one echo per repetition. This technique can be very easily modified to accommodate thinner slices with the same in-plane resolution. The 10 mm slice thickness was used to ensure full coverage of the tumors with the six-slice protocol.

Some healthy volunteer scans were performed as single-slice scans with a 24×24 phase encoding matrix. One FOV of 240×240 mm^2 (10×10×10 mm^3/voxel) and another at 140×140 mm^2 or 160×160 mm^2 (5.83×5.83×10 mm^3/voxel or 6.67×6.67×10 mm^3/voxel respectively) were chosen to compare different nominal spatial resolutions. The TR was kept constant at 1200 - 1500 ms for both the high- and low-resolution scans of each volunteer.

3.3 Results:

Figures 3-7(a) and 3-7(b) show the imaging grids of the low-resolution and high-resolution spectroscopic imaging scans respectively. The difference in the coverage of the head by the different FOVs is shown. High resolution quality is achieved by keeping the same number of phase encodes as the low resolution while

covering a smaller FOV. Since the high-resolution scan is not covering the whole head, the resulting image may suffer from aliasing artifacts. To reduce aliasing artifacts, crusher gradients were used to suppress the signal outside the VOI.

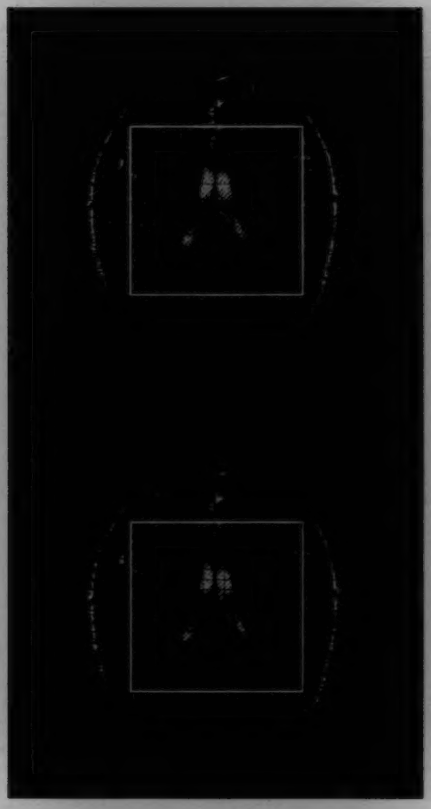

Figure (3-7): The Spectroscopic Imaging grids (FOVs) for (a) the low–resolution ($9.5\times9.5\times10\ mm^3$/voxel) scan (b) the high-resolution ($5.83\times5.83\times10 mm^3$/voxel) scan. VOI shown as the green shaded region in the centre.

Figures 3-8(a) and 3-8(b) show the scan grids and corresponding spectra for both MRSI scans. The spectra of the high-resolution scan have a lower signal to noise ratio than those of the low-resolution scan, however, the three metabolite peaks are visible on all the shown spectra.

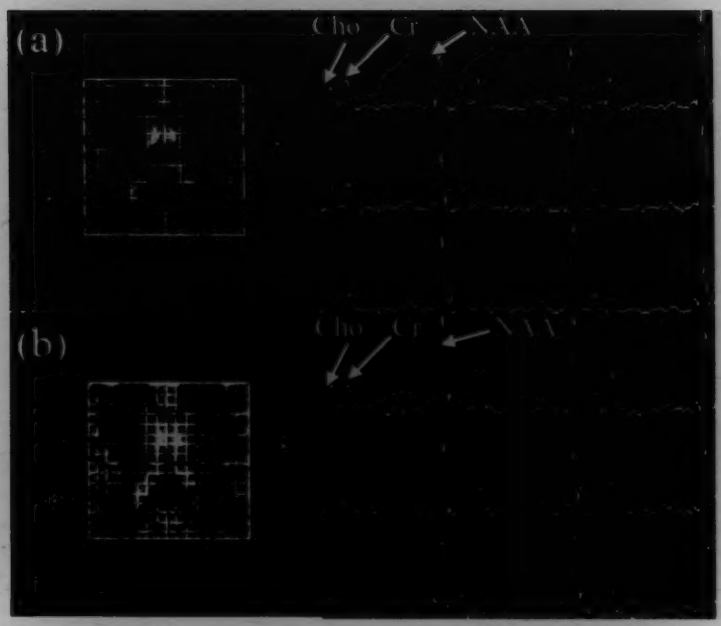

Figure (3-8): (a) single slice, TR 1500 ms low-resolution (9.5×9.5×10 mm^3/voxel) scan. Left: VOI. Right: Spectra corresponding to outlined voxels. The visible peaks left-right are Cho, Cr, NAA; (b) single slice, TR 1500 ms high-resolution (5.83×5.83×10 mm^3/voxel) scan. Left: VOI. Right: Spectra corresponding to outlined voxels. The visible peaks left-right are Cho, Cr, NAA.

Figure 3-9 shows the uninterpolated (24×24 pixels) metabolite maps calculated on Matlab. The images show the relative Cr signal scaled to the highest Cr signal in the each image. Although the resolution of both images is poor compared to anatomic MRI images, the ventricles appear to be more blurred in the low resolution maps.

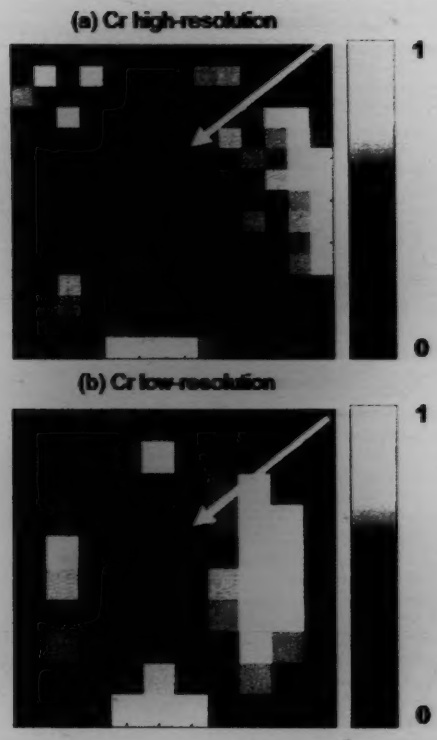

Figure (3-9): Volunteer creatine maps acquired with TR 1200 ms at (a) high-resolution (6.25×6.25×10mm^3/voxel) and (b) low-resolution (10×10×10mm^3/voxel). The maps are scaled individually and the colorbar represents relative intensity. The arrow identifies the ventricles.

3.3.1 SNR Study

Figure 3-3 shows sample speetra acquired form the uniform phantom with voxel sizes ranging from 10×10×10 mm^3 to 3.33×3.33×10 mm^3. Figure 3-10 shows the average SNR calculated over the ROI for the different voxel sizes. The low resolution (10×10×10 mm^3) and the high resolution (5×5×10 mm^3) have SNR's of 1484.3 and 748.8 respectively.

For both scans, the mean creatine peak height is more than 2 standard deviations greater than the mean noise level satisfying our criterion for having an acceptable SNR.

The graph also shows the same for the *in-vivo* scans with the low and high resolutions. Therefore it can be safely stated that for all the presented resolutions the user and the fitting algorithm would be able to clearly distinguish between the metabolite peaks and the noise.

Based on the comparison with the phantom studies, one might expect that the volunteer low-resolution scan would have a higher SNR than measured (385.5). However, the SNR is understandably low due to the shorter T2 times of the *in-vivo* metabolites compared to the phantom, non-uniformity of brain tissue, and the poor statistics which is reflected in the high standard deviation. Although peak broadening shouldn't have an effect on our definition of SNR, average FWHM for phantoms is 5.4 Hz, while for volunteers it is 7.3 Hz.

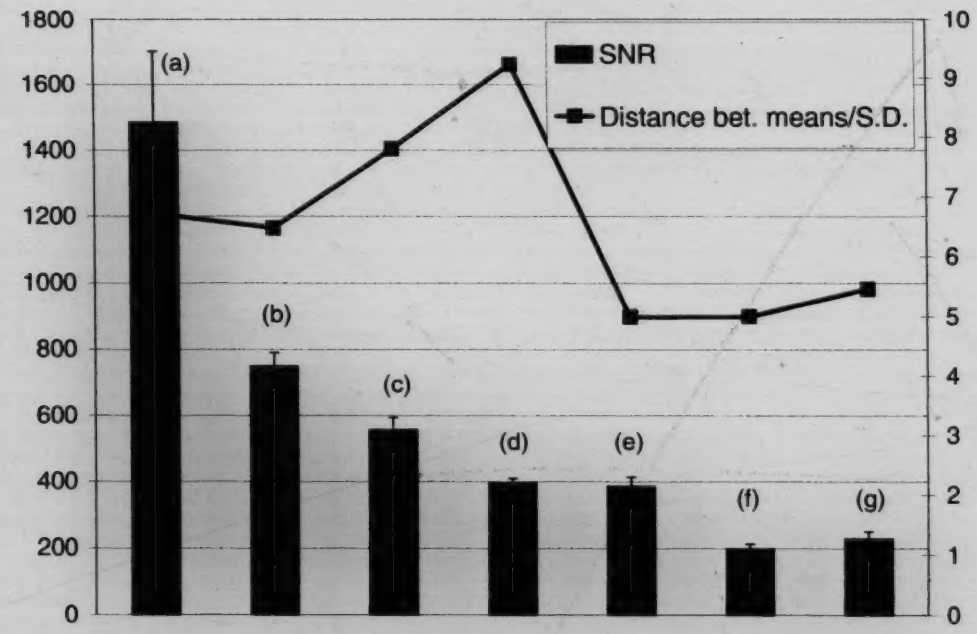

Figure (3-10): SNR study results. (a) Phantom (10×10×10 mm^3/voxel). (b) Phantom (5×5×10 mm^3/voxel). (c) Phantom (4.17×4.17×10 mm^3/voxel). (d) Phantom (3.33×3.33×10 mm^3/voxel). (e) Volunteer low resolution (9.58×9.58×10 mm^3/voxel). (f) Volunteer high resolution (5.83×5.83×10 mm^3/voxel). (g) Volunteer high resolution (5×5×10 mm^3/voxel). The left vertical scale corresponds to the bar graph representing the SNR, while the right vertical scale corresponds to the line graph representing the number of standard deviations separating the mean Cr height and mean noise level.

3.3.2 Effects of Voxel Size on Metabolite Ratios

Using the same uniform phantom and scans used for the *in-vitro* SNR study, the effect of voxel size on metabolite ratios was investigated. (*section 3.2.4.2)*

Figure 3-12 shows the mean Cho/Cr ratio within the ROI for each spatial resolution. The mean ratio calculated for the high resolution ($5\times5\times10$ mm^3) and the low resolution ($10\times10\times10$ mm^3) agree within one standard deviation. Therefore, our high-resolution scans can be used to reproduce reliable Cho/Cr ratios. Since, the decrease in voxel size affects the signal from all metabolites equally; it is also safe to assume that our high-resolution scans can be used to reliably reproduce any metabolite ratios.

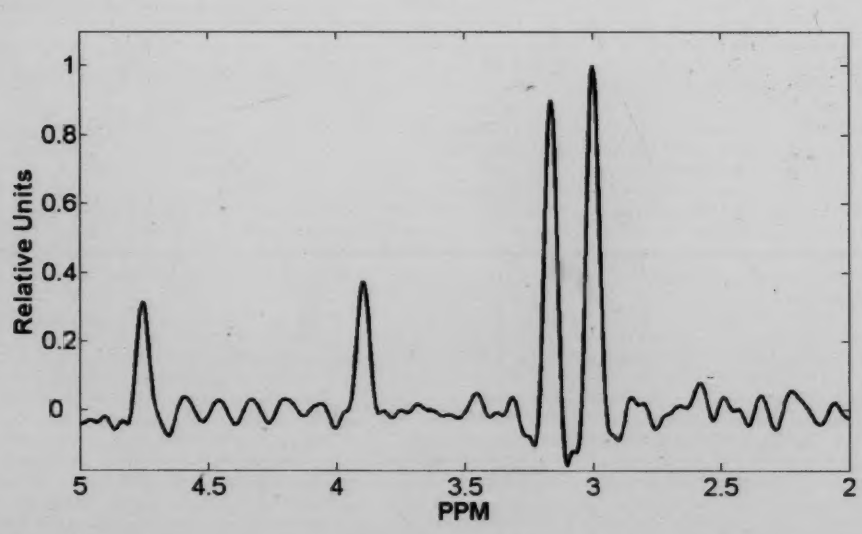

Figure (3-11): Typical spectrum from the uniform phantom used for the SNR and metabolite ratio studies. The peaks of interest are Cho and Cr at 3.2 ppm and 3.0 ppm respectively.

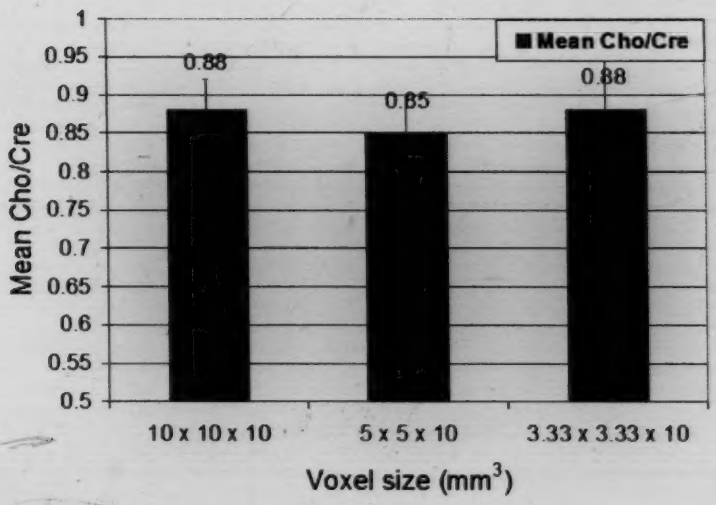

Figure (3-12): Effects of voxel size on metabolite ratios.

3.3.3 Clinical Subject Studies

Figure (3-13) shows sample spectra acquired using the optimized 6-slice scanning sequence on a clinical Glioblastoma Multiforme subject post-surgery (ETH 21780, Cross Cancer Institute, Multimodality functional imaging (MRSI and dynamic contrast enhancement MRI) predicts tumor migration, invasiveness, and patterns of failure of human Glioblastoma treated with concurrent radiation therapy and Temozolomide, Principal Investigator: B. Abdulkarim). The figure shows two sample spectra, the first corresponding to a voxel within the tumor while the second corresponds to normal tissue. As expected, the first spectrum shows elevated levels of choline and very low levels of NAA and Cr compared to the normal tissue spectrum.

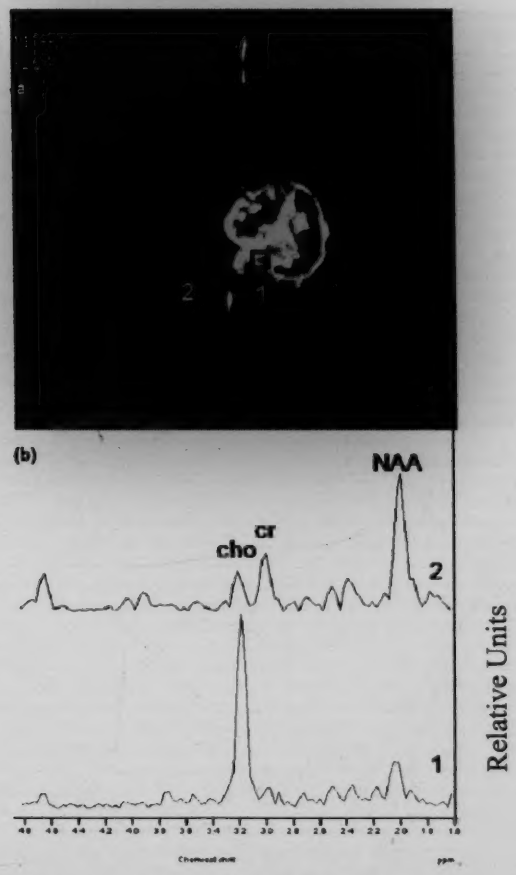

Figure (3-13): (a) T1-weighted post-contrast image of a clinical GBM subject post-surgery. *(b) MRSI spectra corresponding to a clinical GBM subject. Spectrum #1 corresponds to a point inside the tumor as shown by the contrast enhancement in the anatomic image. Spectrum #2 corresponds to a point within the healthy tissue.*

3.3.4 *Comparison* of High-Resolution vs. Low-Resolution MRSI

Figures 3-14(a) and 3-14(b) show the comparison masks of the spectroscopic scans to the anatomic image at a Cho/Cr ratio $\geq$ 1.75. It was noticed that the contoured volumes depended heavily on the ratio chosen. This is due to linear

interpolation applied to the images from 24×24 pixels to 256×256 pixels. The interpolation process spread the gradient of the ratio values from a steep gradient to a shallow gradient. For this reason, we decided to compare the high and low resolutions over a range of ratio.

The inherently larger voxels corresponding to the low-resolution scans cause the following partial volume effects as shown in Fig. 3-14(b). Firstly, in the low detail region, the boundaries of the simulated tumor shown by the spectroscopic scan are blurred and over estimated. Similarly, but in a reverse fashion, the high detail region of the phantom is not accurately represented because of the surrounding dominant signal. Those shortcomings appear less drastic in Fig. 3-14(a) where the boundaries of the spectroscopic scan appear to conform better to the geometry of the simulated tumor.

Figure 3-15 shows a graph of the average number of pixels in excess or missed in the spectroscopic scans for the different Cho/Cr ratios. For all three, the percentage of excess and missed pixels of the high-resolution scans is lower than that of the low-resolution scans. As expected, the high-resolution scans provide better conformance to the physical extent of the simulated tumor. The improvement over the low resolution is particularly clear in the high detail region of the phantom.

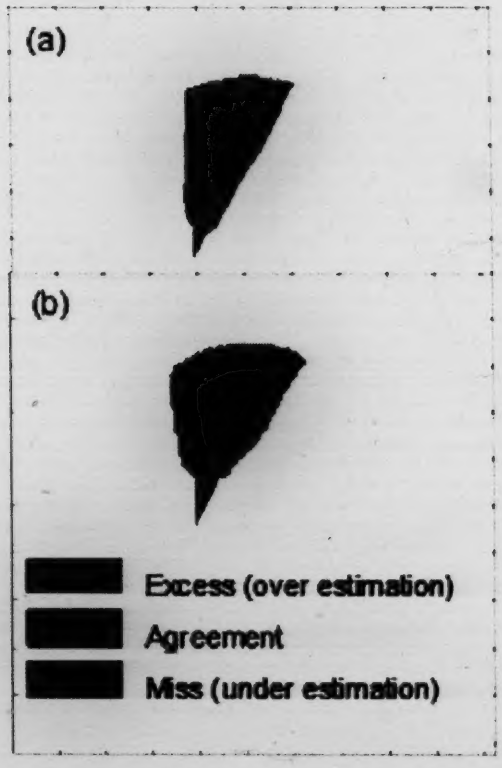

Figure (3-14): Comparison of the spectroscopic scan mask at Cho/Cr ratio of 1.75 to the anatomic (actual) scan of the wedge phantom. (a) High-resolution (5×5×10 mm^3/voxel) scan. (b) Low-resolution (10×10×10 mm^3/voxel) scan. Notice the difference in phantom coverage especially in the high detail region of the phantom. Also notice the blurring and over estimation of the phantom size in the low detail region.

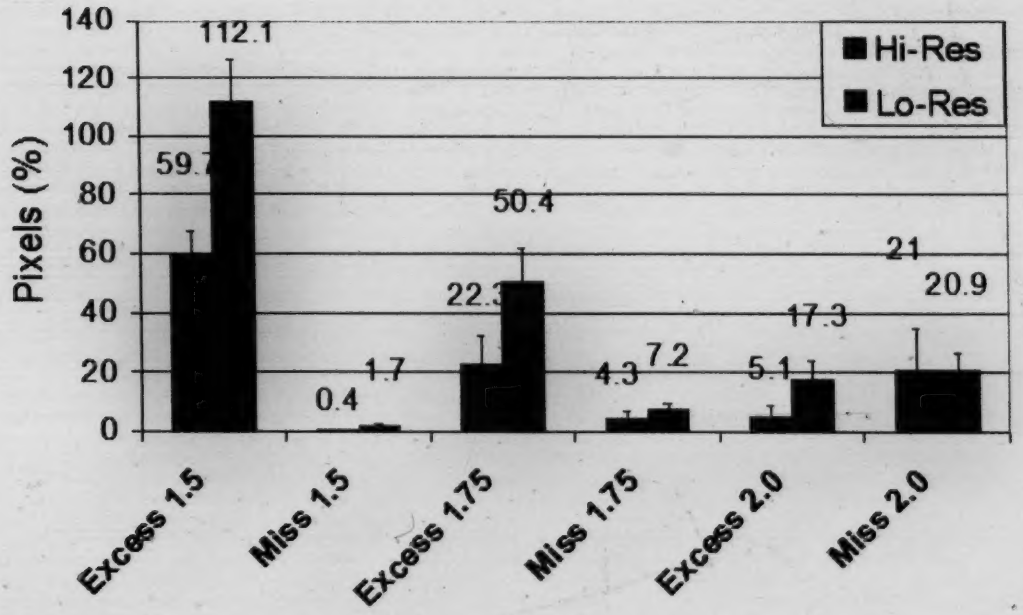

Figure (3-15): Bar graph comparing the results of the quantitative comparison between high-resolution (5×5×10 mm^3/voxel) and low-resolution (10×10×10 mm^3/voxel) scans of the wedge phantom. Notice the high-resolution scans always yield less misses and excess pixels than the low-resolution scans at all thresholds.

Low Diffusion Phantoms

Similar to the results shown above, Figs. 3-16 and 3-17 show that for both the low-diffusion wedge phantoms, the high-resolution scans were more conformal to the physical shape of the wedge (at a Cho/NAA ratio ≥ 1).

Since all phantoms showed the same pattern of differences between high- and low-resolution scans, this confirms that diffusion did not have a significant effect on the results. However, a diffusion free phantom would be more accurate and versatile.

One of the ways that can be used to measure the diffusion effects in the phantoms is by filling the wedge-shaped void with a contrast agent (gadolinium). Gadolinium shortens the T1 times of the surrounding molecules. On a T1 weighted scan, the molecules surrounding gadolinium would appear bright due to their decreased T1 times. The phantom would be scanned over a period of time and the contrast enhancement would be compared between the different scans to monitor the diffusion of the contrast agent through the gel.

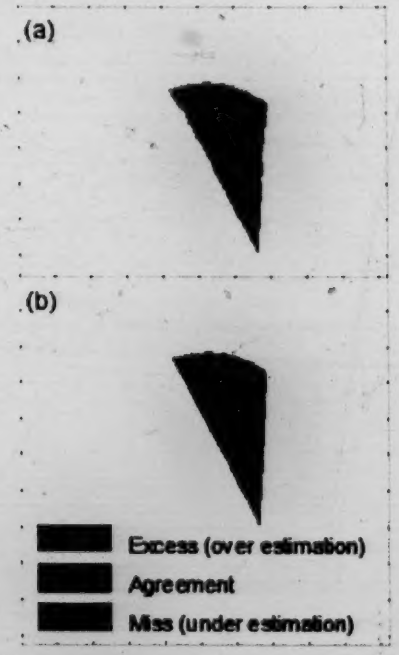

Figure (3-16): 5% by weight porcine gel wedge phantom. Comparison of the spectroscopic scan mask at Cho/NAA ratio of 1 to the anatomic (actual) scan of the wedge phantom. (a) High-resolution (5×5×10 mm^3/voxel) scan. (b) Low-resolution (10×10×10 mm^3/voxel) scan. The high resolution was scanned first then the low resolution followed after 5 minutes.

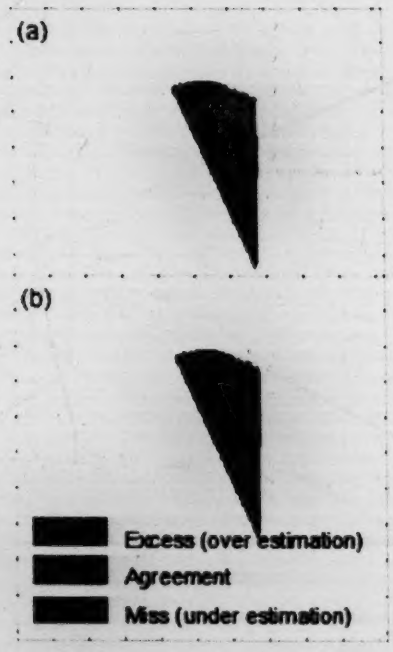

Figure (3-17): 15% by weight porcine gel wedge phantom. Comparison of the spectroscopic scan mask at Cho/NAA ratio of 1 to the anatomic (actual) scan of the wedge phantom. (a) High-resolution (5×5×10 mm^3/voxel) scan. (b) Low-resolution (10×10×10 mm^3/voxel) scan. The low resolution was scanned first then the high resolution followed after 5 minutes.

References:

1. Li, X., Jin, H., Lu, Y., Oh, J., Chang, S., Nelson, S.J., *Identification of MRI and 1H MRSI parameters that may predict survival for patients with malignant gliomas* NMR Biomed. , 2004. 17(1): p. 10-20.
2. Nelson, S.J., Graves, E., Pirzkall, A., Li, X., Chan, A.A., Vigneron, D.B., McKnight, T.R., *In Vivo molecular imaging for planning radiation therapy of gliomas: an application of 1H MRSI.* J. Magn. Reson. Imaging., 2002. 16(4): p. 464-476.
3. Pallud, J., Devaux, B., Nataf, F., Roux, F.X., Daumas-Duport, C., *Spatial delimitation of low grade oligodendrogliomas.* Neurochirurgie. , 2005. 51(3-4): p. 253-259.
4. Pirzkall, A., Li, X., Oh, J., Chang, S., Berger, M.S., Larson, D.A., Verhey, L.J., Dillon, W.P., Nelson, S.J., *3D MRSI for resected high-grade gliomas*

before RT: tumor extent according to metabolic activity in relation to MRI. Int. J. Radiat. Oncol. Biol. Phys., 2004. 59(1): p. 126-137.

5. Walecki, J., Tarasow, E., Kubas, B., Czemicki, Z., Lewko, J., Podgorski, J., Sokol, M., Grieb, P., *Hydrogen-1 MR spectroscopy of the peritumoral zone in patients with cerebral glioma: assessment of the value of the method.* Acad. Radiol., 2003. 10(2): p. 145-153.
6. Chang, J., Thakur, S., Perera, G., Kowalski, A., Huang, W., Karimi, S., Hunt, M., Koutcher, J., Fuks, Z., Amols, H., Narayana, A., *Image-fusion of MR spectroscopic images for treatment planning of gliomas.* Med. Phys., 2006. 33(1): p. 32-40.
7. McKnight, T.R., Noworolski, S.M., Vigneron, D.B., Nelson, S.J., *An automated technique for the quantitative assessment of 3D-MRSI data from patients with glioma.* J. Magn. Reson. Imaging., 2001. 13(2): p. 167-177.
8. Xu, D., Chen, A.P., Cunningham, C., Osorio, J.A., Nelson, S.J., Vigneron, D.B., *Spectroscopic imaging of the brain with phased-array coils at 3.0T.* J. Magn. Reson. Imaging., 2006. 24(1): p. 69-74.
9. Frayne, R., Goodyear, B.G., Dickhoff, P., Lauzon, M.L., Sevick, R.J., *Magnetic resonance imaging at 3.0 tesla: Challenges and advantages in clinical neurological imaging.* Invest. Radiol., 2003. 38(7): p. 385-402.
10. Barker, P.B., Hearshen, D.O., Boska, M.D., *Single-voxel proton MRS of the human brain at 1.5T and 3.0T.* Magn. Reson. Med., 2001. 45(5): p. 765-769.
11. Nishimura, D.G., *Principles of Magnetic Resonance Imaging*. 1996: Stanford University.
12. Fulham, M.J., Bizzi, A., Dietz, M.J., Shih, H.H., Raman, R., Sobering, G.S., Frank, J.A., Dwyer, A.J., Alger, J.R., Chiro, G.D., *Mapping of brain tumor metabolites with proton MR spectroscopic imaging: clinical relevance.* Radiology, 1992. 185(3): p. 675-686.
13. Luyten, P.R., Marien, A.J., Heindel, W., van Gerwen, P.H., Herholz, K., den Hollander, J.A., Friedmann, G., Heiss, W.D., *Metabolic imaging of patients with intracranial tumors: H-1 MR spectroscopic imaging and PET.* Radiology, 1990. 176(3): p. 791-799.
14. Segebarth, C.M., Baleriaux, D.F., Luyten, P.R., Hollander, J.A.d., *Detection of metabolic heterogeneity of human intracranial tumors in vivo by 1H NMR spectroscopic imaging.* Magn. Reson. Med., 1990. 13(1): p. 62-76.
15. Shimizu, H., Kumabe, T., Tominaga, T., Kayama, T., Hara, K., Ono, Y., Sato, K., Arai, N., Fujiwara, S., Yoshimoto, T., *Noninvasive evaluation of malignancy of brain tumors with proton MR spectroscopy.* Am. J. Neuroradiol., 1996. 17(4): p. 737-747.
16. Preul, M.C., Caramanos, Z., Collins, D.L., Villemure, J.G., Leblanc, R., Olivier, A., Pokrupa, R., Arnold, D.L., *Accurate, noninvasive diagnosis of human brain tumors by using proton magnetic resonance spectroscopy.* Nat. Med., 1996. 2(3): p. 323-325.
17. Bottomly, P.A., *Selective volume method for performing localized NMR spectroscopy*, U. Patent, Editor. 1984.

18. Gordon, R.E., Ordidge, R.J. *Volume selection for high resolution NMR studies.* in *Abstracts of the Society of Magnetic Resonance in Medicine 3rd Annual Meeting.* 1984. New York.
19. Ordidge, R.J., Bendall, M.R., Gordon, R.E., Connelly, A., *Magnetic Resonance in Biology and Medicine*, ed. G.Govil, C.L. Khetraplal, and A. Saran. 1985, New Delhi: McGraw-Hill. 387-397.
20. Hennig, J., Nauerth, A., Friedburg, H., *RARE imaging: a fast imaging method for clinical MR.* Magn. Reson. Med., 1986. 3(6): p. 823-833.
21. Doddrell, D.M., Galloway, G., Brooks, W., Filed, J., Bulsing, J., Irving, M., Baddeley, H., *Water signal elimination in vivo, using suppression by mistimed echo and repetitive gradient episodes.* J. Magn. Reson., 1986. 70(1): p. 176-180.
22. Hasse, A., Frahm, J., Hanicke, W., Mattaei, W., *1H NMR chemical shift selective (CHESS) imaging.* Phys. Med. Biol., 1985. 30(4): p. 341-344.
23. Mierisova, S., Ala-Korpela, M., *MR spectroscopy quantitation: a review of frequency domain methods.* NMR Biomed., 2001. 14(4): p. 247-259.
24. Frahm, J., Bruhn, H., Gyngell, M.L., Merboldt, K.D., Hanicke, W., Sauter, R., *Localized proton NMR spectroscopy in different regions of the human brain in vivo. Relaxation times and concentrations of cerebral metabolites.* Magn. Reson. Med., 1989. 11(1): p. 47-63.
25. Rice, J.R., Milbrandt, R.H., Madsen, E.L., Frank, G.R., Boote, E.J., Blechinger, J.C., *Anthropomorphic 1H MRS head phantom.* Med. Phys., 1998. 25(7): p. 1145-1156.
26. Langkowski, J.H., Wieland, J., Bomsdorf, H., Leibfritz, D., Westpha, M., Offermann, W., Maas, R., *Pre-operative localized in vivo proton spectroscopy in cerebral tumors at 4.0 Tesla—First results.* Magn. Reson. Imaging, 1989. 7(5): p. 547-555.

Chapter Four

4 Conclusions and Future Work

4.1 Conclusions:

The advantages that spectroscopic imaging can offer in the therapeutic management of brain tumor are significant. Not only does the metabolic information gathered using MRSI provide a means of non-invasive tumor assessment, it also implies obvious benefits to the use of MRSI in delineating boundaries for radiation treatment of tumors. Such benefits have recently been demonstrated in the literature [1], where the delineation of tumor volume in treatment plans for external beam radiation therapy has been shown to change when MRSI metabolite information was considered. MRSI showed regions of increased tumor activity that were not covered by conventional imaging and contouring techniques.

High-resolution MRSI provides promising high-resolution biochemical information for treatment planning purposes. It provides more spatial information than current MRSI scans used for diagnosis. The spatial correlation with CT and MRI can help in more precise delineation of the tumor volume leading to more conformal treatment plans and less complications.

In radiotherapy, a high-resolution biological imaging tool is long overdue. Because of the advancements in the radiation delivery techniques the biggest

challenge in radiotherapy planning is tumor localization. High-resolution MRSI provides the means of biologically localizing the tumor as well as areas of potential tumor invasion allowing for more conformal plans and possibly dose escalation.[1]

In this work, a technique has been successfully tested for high-resolution MRSI at 3 T that can be used for the brain. It has been demonstrated that for both phantom and volunteer scans, the mean creatine peak height was more than 2 standard deviations greater than the mean noise level. Therefore, despite the decrease in the spectral SNR, the scans met the set criterion for having an acceptable SNR.

It has also been demonstrated that, through our investigation of the effects of voxel size on metabolite ratios, the Cho/Cr ratios obtained from both resolution scans agree to within one standard deviation. Therefore, our high-resolution scans can be used to reproduce reliable Cho/Cr ratios.

The quantitative comparison between both ranges of resolution has shown that high-resolution scans always provided better conformance to the simulated tumor volume especially in the high detail regions.

The multi-slice technique that we described herein is useful over most of the brain volume including the ventricles. However, for tumors located in the posterior or the anterior side of the head, the use of a 3-D PRESS would be more appropriate in order to avoid aliasing artifacts in the VOI.

4.2 Future Work:

As mentioned earlier, the larger objective of the project is to improve MRSI as a means of biochemical identification of brain tumors - GBM - for radiotherapy treatment planning.

An automatic method of delineating tumors using MRSI used by other groups is currently being investigated. McKnight et al. derived a method for automatically differentiating tumors from normal tissue using the choline-to-NAA index (CNI).[2] In their work they show that CNI of 2 is significant of a malignancy. Lately, we have been using a wedge phantom to correlate the physical extent of the tumor with the volume depicted by MRSI. Preliminary results of our CNI calculations show that for the wedge phantom, CNI of 2 fails to accurately depict the geometry of the wedge phantom. Moreover, CNI of 2 falsely indicated malignancies in regions of the phantom where the metabolite concentrations imitated those of healthy tissue. Accordingly, it is suspected that a CNI of 2 is a not the correct threshold to be used to differentiate tumors from healthy tissue.

The proposed future work is to conduct in-depth studies on CNI outcome that would investigate the following:

1. The use of the wedge phantom described in our previous work to study the specificity and sensitivity of the CNI based method introduced by McKnight et al. Also, work will be conducted to optimize the CNI value that would best represent the geometry of the simulated tumor within the phantom.

2. Conducting a series of MRSI scans on healthy volunteers to determine the average CNI corresponding to healthy brain tissue. A baseline would then be established for healthy brain tissue that will be used to identify healthy tissue from tumors on clinical subjects.
3. The biological outcomes such as tumor control probability (TCP) and normal tissue complication probability (NTCP) of incorporating biochemical information offered by MRSI in treatment planning. The optimized CNI will be used to delineate biological target volumes (BTV) on GBM clinical subjects (ETH 21780) under the supervision of the co-supervisor. The resulting volumes will be compared to the gross tumor volumes produced using conventional anatomical imaging based delineation methods. Using in-house developed software based on biological modeling, the expected TCP and NTCP for the different plans will be compared.
4. The patterns of failure and survival in patients where radiotherapy was conducted utilizing a BTV and compare the results to patients treated based on conventional anatomic imaging techniques.

In conclusion, the study and optimization of the CNI as a parameter for tumor delineation improves the accuracy of tumor identification parameters. CNI can provide a solid quantitative basis for biochemical delineation of tumors which may potentially lead to more accurate targeting of microscopic disease, improving outcome and reducing recurrence.

References:

1. Nelson, S.J., Graves, E., Pirzkall, A., Li, X., Chan, A.A., Vigneron, D.B., McKnight, T.R., *In Vivo molecular imaging for planning radiation therapy of gliomas: an application of 1H MRSI.* J. Magn. Reson. Imaging., 2002. **16**(4): p. 464-476.
2. McKnight, T.R., Noworolski, S.M., Vigneron, D.B., Nelson, S.J., *An automated technique for the quantitative assessment of 3D-MRSI data from patients with glioma.* J. Magn. Reson. Imaging., 2001. **13**(2): p. 167-177.

Bibliography

(the page numbers on the side indicate the page in the thesis where the reference is cited)

1. Alexander, E.r., Loeffler, J.S., *Radiosurgery for primary malignant brain tumors.* Semin. Surg. Oncol., 1998. **14**(1): p. 43-52. p. 1

2. Barker, P.B., Hearshen, D.O., Boska, M.D., *Single-voxel proton MRS of the human brain at 1.5T and 3.0T.* Magn. Reson. Med., 2001. **45**(5): p. 765-769. p. 30, 45, 49

3. Bishop, J., Plewes, D. *Stimulated echo effects in fast spin echo images.* in *10th Annual Mtg. Soc. Magn. Reson. In Med.* 1991. San Francisco. p. 113

4. Block, F., *Nuclear induction.* Physical Review, 1946. **70**: p. 460-474. p. 98

5. Bottomly, P.A., *Selective volume method for performing localized NMR spectroscopy*, U. Patent, Editor. 1984. p. 17, 32

6. Bracewell, R.N., *The Fourier Transform and its Applications.* 1978: McGraw-Hill. 122. p. 111

7. Brandes, A., Soesan, M., Fiorentino, M.V., *Medical treatment of high grade malignant gliomas in adults: an overview.* Anticancer Res, 1991. **11**(2): p. 719-727. p. 1

8. Bronskill, M.J. *The physics of MRI.* in *AAPM summer school proceeding.* 1992 Woodbury: American Institute of Physics, Inc. p. 84, 89, 96

9. Brown, M.A., Semelka, R.C., *MRI Basic Principles and Applications.* 1995: John Wiley & Sons. p. 102

10. Chang, J., Thakur, S., Perera, G., Kowalski, A., Huang, W., Karimi, S., Hunt, M., Koutcher, J., Fuks, Z., Amols, H., Narayana, A., *Image-fusion of MR spectroscopic images for treatment planning of gliomas.* Med. Phys., 2006. **33**(1): p. 32-40.

p. 2, 6, 10, 29

11. Combs, S.E., Konkel, S., Schulz-Ertner, D., Munter, M.W., Debus, J., Huber, P.E., Thilmann, C., *Intensity modulated radiotherapy (IMRT) in patients with carcinomas of the paranasal sinuses: clinical benefit for complex shaped target volumes.* Radiat. Oncol., 2006. **1**: p. 23.

p. 10

12. Di Costanzo, A., Scarabino, T., Trojsi, F., Giannatempo, G.M., Popolizio, T., Catapano, D., Bonavita, S., Maggialetti, N., Tosetti, M., Salvolini, U., d'Angelo, V.A., Tedeschi, G., *Multiparametric 3T MR approach to the assessment of cerebral gliomas: tumor extent and malignancy.* Neuroradiology, 2006. **48**(9): p. 622-631.

p. 5, 6, 10

13. Doddrell, D.M., Galloway, G., Brooks, W., Filed, J., Bulsing, J., Irving, M., Baddeley, H., *Water signal elimination in vivo, using suppression by mistimed echo and repetitive gradient episodes.* J. Magn. Reson., 1986. **70**(1): p. 176-180.

p. 40

14. Fine, H.A., Dear, K.B., Loeffler, J.S., Black, P.M., Canellos, G.P., *Meta-analysis of radiation therapy with and without adjuvant chemotherapy for malignant gliomas in adults.* Cancer, 1993. **71**(8): p. 2585-2597.

p. 1

15. Frahm, J., Bruhn, H., Gyngell, M.L., Merboldt, K.D., Hanicke, W., Sauter, R., *Localized proton NMR spectroscopy in different regions of the human brain in vivo. Relaxation times and concentrations of cerebral metabolites.* Magn. Reson. Med., 1989. **11**(1): p. 47-63.

p. 17, 52

16. Frayne, R., Goodyear, B.G., Dickhoff, P., Lauzon, M.L., Sevick, R.J., *Magnetic resonance imaging at 3.0 tesla: Challenges and advantages in clinical neurological imaging.* Invest. Radiol., 2003. **38**(7): p. 385-402.

p. 30

17. Freeman, R., *Shaped freuqncy pulses in high resolution NMR.* J. of Progress in NMR Spectroscopy, 1998. **32**: p. 59-106.
p. 109

18. Fulham, M.J., Bizzi, A., Dietz, M.J., Shih, H.H., Raman, R., Sobering, G.S., Frank, J.A., Dwyer, A.J., Alger, J.R., Chiro, G.D., *Mapping of brain tumor metabolites with proton MR spectroscopic imaging: clinical relevance.* Radiology, 1992. **185**(3): p. 675-686.
p. 32

19. Fuller, C.D., Thomas, C.R.J., Wong, A., Cavanaugh, S.X., Salter, B.J., Herman, T.S., Fuss, M., *Image-guided intensity-modulated radiation therapy for gallbladder carcinoma.* Radiother. Oncol., 2006. **81**(1): p. 65-72.
p. 10

20. Gordon, R.E., Ordidge, R.J. *Volume selection for high resolution NMR studies.* in *Abstracts of the Society of Magnetic Resonance in Medicine 3rd Annual Meeting.* 1984. New York.
p. 17, 32

21. Haacke, E.M., *Magnetic Resonance Imaging, physics principles and sequence design.* 1999: John Willey & Sons.
p. 23, 24, 85, 86, 101, 113

22. Hasse, A., Frahm, J., Hanicke, W., Mattaei, W., *1H NMR chemical shift selective (CHESS) imaging.* Phys. Med. Biol., 1985. **30**(4): p. 341-344.
p. 40

23. Hennig, J., Nauerth, A., Friedburg, H., *RARE imaging: a fast imaging method for clinical MR.* Magn. Reson. Med., 1986. **3**(6): p. 823-833.
p. 33

24. Hess, C.F., Schaaf, J.C., Kortmann, R.D., Schabet, M., Bamberg, M., *Malignant glioma: patterns of failure following individually tailored limited volume irradiation.* Radiother. Oncol., 1994. **30**(2): p. 146-149.
p. 1, 7

25. Hinshaw, W.S. *An introduction to NMR imaging.* in *Proceeding of the IEEE.* 1983.
p. 92

26. Kantor, G., Loiseau, H., Vital, A., Mazeron, J.J., *Gross tumor volume (GTV) and clinical target volume (CTV) in adult gliomas.* Cancer Radiother., 2001. **5**(5): p. 571-580.
p. 7

27. Kristiansen, K., Hagen, S., Kollevold, T., Torvik, A., Holme, I., Nesbakken, R., Hatlevoll, R., Lindgren, M., Brun, A., Lindgren, S., Notter, G., Andersen, A.P., Elgen, K., *Combined modality therapy of operated astrocytomas grade III and IV. Confirmation of the value of postoperative irradiation and lack of potentiation of bleomycin on survival time: a prospective multicenter trial of the Scandinavian Glioblastoma Study Group.* Cancer, 1981. **47**(4): p. 649-653.

p. 1

28. Kwee, S.A., Coel, M.N., Lim, J., Ko, J.P., *Combined use of F-18 fluorocholine positron emission tomography and magnetic resonance spectroscopy for brain tumor evaluation.* J. Neuroimaging, 2004. **14**(3): p. 285-289.

p. 2

29. Langkowski, J.H., Wieland, J., Bomsdorf, H., Leibfritz, D., Westpha, M., Offermann, W., Maas, R., *Pre-operative localized in vivo proton spectroscopy in cerebral tumors at 4.0 Tesla—First results.* Magn. Reson. Imaging, 1989. **7**(5): p. 547-555.

p. 52

30. Lassen, U., Kristjansen, P.E., Wagner, A., Kosteljanetz, M., Poulsen, H.S., *Treatment of newly diagnosed glioblastoma multiforme with carmustine, cisplatin and etoposide followed by radiotherapy. A phase II study.* J Neurooncol., 1999. **42**(2): p. 161-166.

p. 1

31. Lee, S.W., Fraass, B.A., Marsh, L.H., Herbort, K., Gebarski, S.S., Martel, M.K., Radany, E.H., Lichter, A.S., Sandler, H.M., *Patterns of failure following high-dose 3-D conformal radiotherapy for high-grade astrocytomas: a quantitative dosimetric study.* Int. J. Radiat. Oncol. Biol. Phys., 1999. **43**(1): p. 79-88.

p. 1, 7

32. Li, X., Jin, H., Lu, Y., Oh, J., Chang, S., Nelson, S.J., *Identification of MRI and 1H MRSI parameters that may predict survival for patients with malignant gliomas* NMR Biomed. , 2004. **17**(1): p. 10-20.

p. 20, 28, 32

33. Ling, C.C., Humm, J., Larson, S., Amols, H., Fuks, Z., Leibel, S., Koutcher, J.A., *Towards multidimensional radiotherapy (MD-CRT): biological imaging and biological conformality.* Int. J. Radiat. Oncol. Biol. Phys. , 2000. **47**(3): p. 551-560.

p. 2, 8

34. Luyten, P.R., Marien, A.J., Heindel, W., van Gerwen, P.H., Herholz, K., den Hollander, J.A., Friedmann, G., Heiss, W.D., *Metabolic imaging of patients with intracranial tumors: H-1 MR spectroscopic imaging and PET.* Radiology, 1990. **176**(3): p. 791-799.

p. 32

35. McKnight, T.R., Noworolski, S.M., Vigneron, D.B., Nelson, S.J., *An automated technique for the quantitative assessment of 3D-MRSI data from patients with glioma.* J. Magn. Reson. Imaging., 2001. **13**(2): p. 167-177.

p. 2, 29, 72

36. McRobbie, D.W., *Investigation of the slice characteristics in NMR imaging.* Phys. Med. Biol., 1986. **31**(6): p. 613-626.

p. 105

37. Mierisova, S., Ala-Korpela, M., *MR spectroscopy quantitation: a review of frequency domain methods.* NMR Biomed., 2001. **14**(4): p. 247-259.

p. 41, 42, 48

38. Nelson, S.J., Graves, E., Pirzkall, A., Li, X., Chan, A.A., Vigneron, D.B., McKnight, T.R., *In Vivo molecular imaging for planning radiation therapy of gliomas: an application of 1H MRSI.* J. Magn. Reson. Imaging., 2002. **16**(4): p. 464-476.

p. 2, 5, 10, 28, 31, 32, 44, 70, 71

39. Nishimura, D.G., *Principles of Magnetic Resonance Imaging.* 1996: Stanford University.

p. 15, 16, 23, 24, 25, 26, 31, 32, 35, 99, 110, 112, 113

40. Ordidge, R.J., Bendall, M.R., Gordon, R.E., Connelly, A., *Magnetic Resonance in Biology and Medicine*, ed. G.Govil, C.L. Khetraplal, and A. Saran. 1985 New Delhi: McGraw-Hill. 387-397.

p. 17, 32

41. Pallud, J., Devaux, B., Nataf, F., Roux, F.X., Daumas-Duport, C., *Spatial delimitation of low grade oligodendrogliomas.* Neurochirurgie. , 2005. **51**(3-4): p. 253-259.

p. 2, 28

42. Pirzkall, A., Li, X., Oh, J., Chang, S., Berger, M.S., Larson, D.A., Verhey, L.J., Dillon, W.P., Nelson, S.J., *3D MRSI for resected high-grade gliomas before RT: tumor extent according to metabolic activity in relation to MRI.* Int. J. Radiat. Oncol. Biol. Phys., 2004. **59**(1): p. 126-137.

p. 2, 8, 10, 28, 34

43. Preul, M.C., Caramanos, Z., Collins, D.L., Villemure, J.G., Leblanc, R., Olivier, A., Pokrupa, R., Arnold, D.L., *Accurate, noninvasive diagnosis of human brain tumors by using proton magnetic resonance spectroscopy.* Nat. Med., 1996. **2**(3): p. 323-325.

p. 32

44. Purcell, E.M., Torrey, H.C., Pound, R.B., *Resonance absorption by nuclear magnetic moments in a solid.* Physical Review, 1946. **69**: p. 37-38.

p. 98

45. Rades, D., Fehlauer, F., Wroblesky, J., Albers, D., Schild, S.E., Schmidt, R., *Prognostic factors in head-and-neck cancer patients treated with surgery followed by intensity-modulated radiotherapy (IMRT), 3D-conformal radiotherapy, or conventional radiotherapy.* Oral Oncol., 2006. doi:10.1016/j.oraloncology.2006.05.006.

p. 10

46. Rice, J.R., Milbrandt, R.H., Madsen, E.L., Frank, G.R., Boote, E.J., Blechinger, J.C., *Anthropomorphic 1H MRS head phantom.* Med. Phys., 1998. **25**(7): p. 1145-1156.

p. 52

47. Segebarth, C.M., Baleriaux, D.F., Luyten, P.R., Hollander, J.A.d., *Detection of metabolic heterogeneity of human intracranial tumors in vivo by 1H NMR spectroscopic imaging.* Magn. Reson. Med., 1990. **13**(1): p. 62-76.

p. 32

48. Shimizu, H., Kumabe, T., Tominaga, T., Kayama, T., Hara, K., Ono, Y., Sato, K., Arai, N., Fujiwara, S., Yoshimoto, T., *Noninvasive evaluation of malignancy of brain tumors with proton MR spectroscopy.* Am. J. Neuroradiol., 1996. **17**(4): p. 737-747.

p. 32

49. Thomas, S.D., *Transient magnetization MRA at 3.0 Tesla*, in *Biomedical Engineering.* 2001, University of Alberta: Edmonton.

p. 89, 99, 113

50. Van Dyk, J., *The Modern Technology of Radiation Onocology.* 1999: Medical Physics Publishing.

p. 1, 8

51. Walecki, J., Tarasow, E., Kubas, B., Czemicki, Z., Lewko, J., Podgorski, J., Sokol, M., Grieb, P., *Hydrogen-1 MR spectroscopy of the peritumoral zone in patients with cerebral glioma: assessment of the value of the method.* Acad. Radiol., 2003. **10**(2): p. 145-153.
p. 2, 28

52. Wallner, K.E., Galicich, J.H., Krol, G., Arbit, E., Malkin, M.G., *Patterns of failure following treatment for glioblastoma multiforme and anaplastic astrocytoma.* Int. J. Radiat. Oncol. Biol. Phys., 1989. **16**(6): p. 1405-1409.
p. 1, 10

53. Xu, D., Chen, A.P., Cunningham, C., Osorio, J.A., Nelson, S.J., Vigneron, D.B., *Spectroscopic imaging of the brain with phased-array coils at 3.0T.* J. Magn. Reson. Imaging., 2006. **24**(1): p. 69-74.
p. 29

54. Zelefsk, M.J., Chan, H., Hunt, M., Yamada, Y., Sippy, A.M., Amols, H., *Long-term outcome of high dose intensity modulated radiation therapy for patients with clinically localized prostate cancer.* J. Urol., 2006. **176**(4): p. 1415-1419.
p. 10

Appendix I: Theory of MRI

Introduction:

In Chapter One we have introduced how the role that MRI plays in the radiotherapy process and how biological imaging using MRSI can improve the outcome of radiotherapy. This Appendix proceeds with an explanation of the basic physics of MRI with the relaxation mechanisms and spatial encoding techniques.

The physics of MRI can be described using both classical and quantum mechanics. While the classical description is simpler to understand, the quantum mechanical aspects of MRI will be introduced to describe the basic theory of the preparation stage. Since the classical description will be used for the whole chapter, the quantum mechanical description of the preparation stage will be discussed first so as not to disrupt the continuity of the chapter.

Quantum Mechanical Description of NMR

Consider a system consisting primarily of protons with spin ½ as our sample for the NMR experiment.

Spin ½ in a static magnetic field (preparation):

The magnetic dipole moment μ of nuclei is related to the spin angular momentum I of the nuclei through:

$$\mu = \gamma h I \qquad \text{(A-1)}$$

where γ is the gyromagnetic ratio of the nuclei and h is Plank's constant. For hydrogen protons, γ= 6.796 radians/(second · Tesla).

The interaction energy of a magnetic dipole moment in a static magnetic field is defined by:

$$E = -\boldsymbol{\mu} \bullet \boldsymbol{B}_0 \qquad \text{(A-2)}$$

where $\boldsymbol{B}_0$ is the static uniform magnetic field.

For hydrogen nuclei in a static uniform field oriented along the Z direction, Eq. A-2 becomes:

$$E = -\gamma h \boldsymbol{I}_z \bullet \boldsymbol{B}_0 \qquad \text{(A-3)}$$

That can be written in operator form using the Hamiltonian which describes the interaction of the spin with the main magnetic field (Zeeman Hamiltonian) as:

$$H_{B_0} = \gamma h B_0 \boldsymbol{I}_z \qquad \text{(A-4)}$$

Applying the Zeeman Hamiltonian to the energy eigenstates in the spin wave function we get the energy eingenvalues corresponding to those eigenstates:

$$H_{B0}(|\alpha\rangle + |\beta\rangle) = E(|\alpha\rangle + |\beta\rangle) = \gamma h B_0 / 2|\alpha\rangle + -\gamma h B_0 / 2|\beta\rangle \qquad \text{(A-5)}$$

where $|\alpha\rangle$ and $|\beta\rangle$ are spins oriented parallel and anti-parallel to B_0 respectively. Accordingly, when a spin ½ system is placed in a uniform static magnetic field there are only two possible energy states in which the spin can be described. The whole system can either be a mixture of those states or purely one or the other.[1]

From Eq. A-5 the Zeeman energy separation between the eigenstates can also be written as:

$$\Delta E = \gamma h B_0$$
$$\Delta E = h\omega_0 \qquad \text{(A-6)}$$

where ω_0 is referred to the as the Larmor frequency and is:

$$\omega_0 = \gamma B_0 \qquad \text{(A-7)}$$

At 3T, ω= 20.388 radian/second.

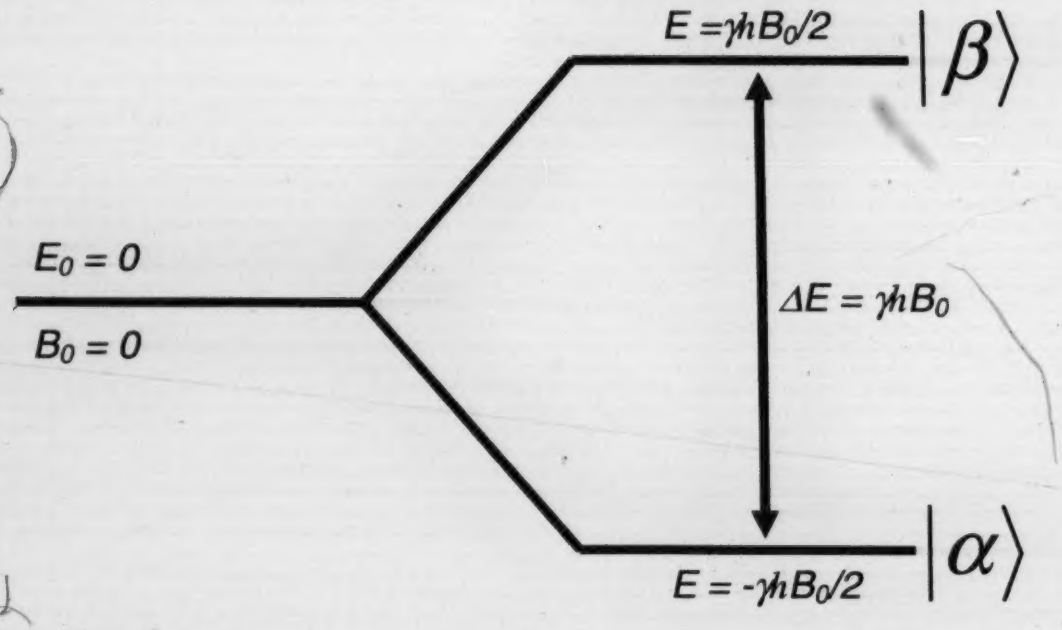

Figure (A-1): The energy level diagram of a spin ½ system observed in $B_0 = 0$ and $B_0 \neq 0$

In thermal equilibrium. the Boltzman distribution defines the relative populations of the spins in the eigenstates [2]:

$$N_{|\beta\rangle} / N_{|\alpha\rangle} = e^{-\Delta E / kT} \qquad \text{(A-8)}$$

where N is the spin population, k is Boltzman constant (1.38×10^{-23} J/K) and T is the temperature in Kelvin.

In the absence of the magnetic field, the spins have equal probability to be oriented in any direction resulting in a net magnetization of zero. However, in the

presence of a static magnetic field, the spins will preferentially orient themselves parallel to the field which results in a net longitudinal magnetization.

The classical description of NMR:

Consider a volume containing an arbitrary sample of protons each with magnetic moment μ. The net magnetization within the sample volume is equal to the sum of the magnetic moment vectors of the protons in the sample:

$$M_0 = \sum_{volume} \mu_i \qquad \text{(A-10)}$$

In the absence of a magnetic field the magnetic moment vectors are oriented randomly as shown in Fig. A-3a. Accordingly, the magnetic moment vectors cancel each other in vectorial sum and the net magnetization of the sample is zero.[2]

Magnetic moments in a stationary magnetic field B_0:

In thermal equilibrium in the presence of a static magnetic field B_0 the magnetic moments of the protons present in our sample would align themselves in a direction either parallel or anti-parallel to the magnetic field. As we discussed earlier, the number of spins in the parallel orientation will be greater than the number of spins in the anti-parallel orientation resulting in a net magnetization along the direction of the applied static magnetic field.

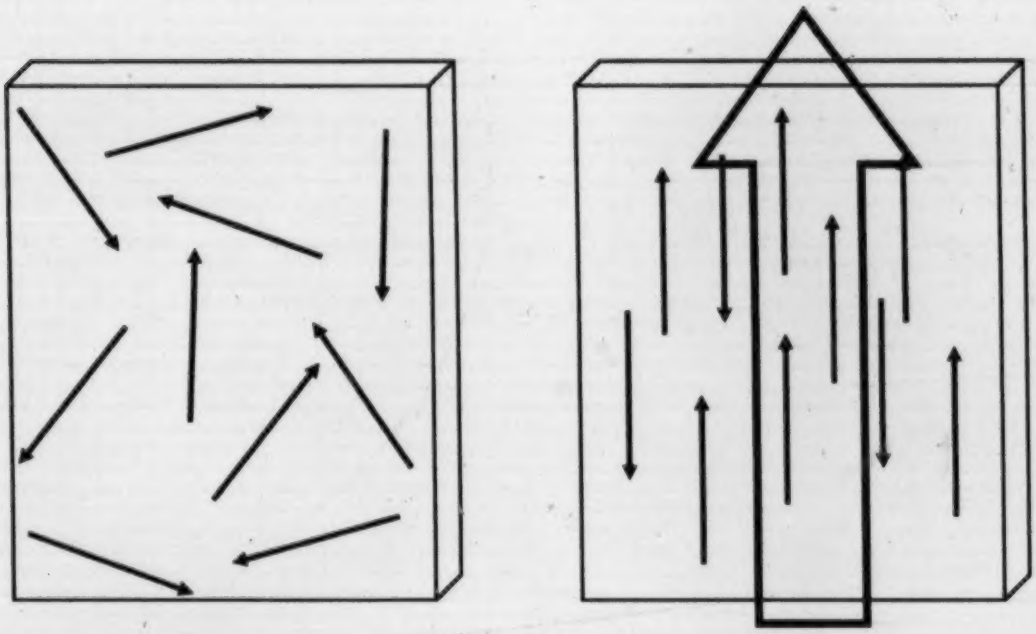

Figure (A-2): magnetic moment vector within a sample shown in: a. The absence of a uniform external magnetic field resulting in random orientations zero net magnetization. b. The magnetic moments are arranged in the parallel and anti-parallel orientation with respect to the applied magnetic field. The net magnetization vector M_0 resulting is shown as the big arrow.

Following the preparation phase, the two remaining stages of excitation and acquisition are executed to complete the MRI experiment.

Description of the excitation process:

The excitation process is achieved by applying a circularly polarized (rotating) magnetic field B_1 with frequency ω B_1 is applied by a radio-frequency (RF) pulse in

the presence of and orthogonal to the static magnetic field $\boldsymbol{B_0}$. The total magnetic field $\boldsymbol{B}$ experienced by the spins then becomes:

$$\boldsymbol{B} = \boldsymbol{B_0} + \boldsymbol{B_1}(t) \qquad \text{(A-11)}$$

where $\boldsymbol{B_0} = (0,0,B_0)$ and $\boldsymbol{B_1} = (B_1 \cos \omega t, B_1 \sin \omega t, 0)$ resulting in:

$$\boldsymbol{B} = (B_1 \cos \omega t, B_1 \sin \omega t, B_0) \qquad \text{(A-12)}$$

where the z-axis is defined along the axis of $\boldsymbol{B_0}$ and the xy-plane is the transverse plane.

Equating the rate of change of angular momentum to the torque experienced by those vectors:

$$h d\boldsymbol{I} / dt = \boldsymbol{\mu} \times \boldsymbol{B} \qquad \text{(A-13)}$$

From Eq. A-1, we obtain:

$$d\boldsymbol{\mu} / dt = \gamma \boldsymbol{\mu} \times \boldsymbol{B} \qquad \text{(A-14)}$$

From Eq. A-10 the equation of motion now becomes:

$$\frac{d}{dt}(\sum \boldsymbol{\mu}) = d\boldsymbol{M}/dt = \gamma \sum \boldsymbol{\mu} \times \boldsymbol{B}$$

$$d\boldsymbol{M}/dt = \gamma \boldsymbol{M} \times \boldsymbol{B} \tag{A-15}$$

$$d\boldsymbol{M}/dt = \gamma \begin{vmatrix} \hat{i} & \hat{j} & \hat{k} \\ M_x & M_y & M_z \\ B_1 \cos \omega t & B_1 \sin \omega t & B_0 \end{vmatrix}, \tag{A-16}$$

which can be written as:

$$\begin{aligned} dM_x/dt &= \gamma(M_y B_0 - M_z B_1 \sin \omega t) \\ dM_y/dt &= \gamma(M_z B_1 \cos \omega t - M_x B_0) \\ dM_z/dt &= \gamma(M_x B_1 \sin \omega t - M_y B_1 \cos \omega t) \end{aligned} \tag{A-17}$$

Thus the motion of the magnetization vector become fairly complex since it involves rotation around the z-axis superimposed on rotation about the transverse axes. In order to better visualize the motion of $\boldsymbol{M}$ and to simplify the mathematics we will consider another reference frame than the Cartesian laboratory frame. The new reference frame is a rotating reference frame rotating with frequency ω equal to that of the circularly polarized $\boldsymbol{B_1}$.[1, 3] In the rotating frame now both $\boldsymbol{B_1}$ and $\boldsymbol{B_0}$ appear to be static in the xy-plane and z-axis respectively.

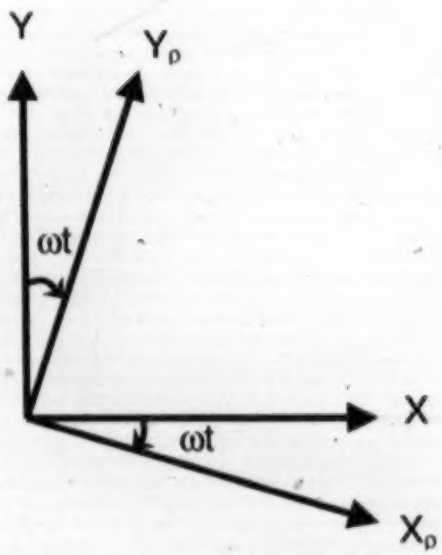

Figure (A-3): the rotating frame of reference ($X_\rho Y_\rho$) with respect to the laboratory frame (X,Y). The rotating frame rotates about the z-axis therefore, Z_ρ is equivalent to Z.

From Fig. A-3, the components of the magnetization vector $\boldsymbol{M}_\rho$ in the rotating frame are related to the magnetization vector $\boldsymbol{M}$ in the laboratory frame through:

$$\begin{aligned} M_{x\rho} &= M_x \cos \omega t + M_y \sin \omega t \\ M_{y\rho} &= -M_x \sin \omega t + M_y \cos \omega t \\ M_{z\rho} &= M_z \end{aligned} \qquad \text{(A-18)}$$

The derivation of these equations and substitution with the derivatives in the laboratory frame from Eq. A-17 now yield the equations of motion in the rotating frame:

$$dM_{xp}/dt = (\gamma B_0 + \omega)M_{yp}$$
$$dM_{yp}/dt = -(\gamma B_0 + \omega)M_{xp} + \gamma B_1 M_{zp} \qquad \text{(A-19)}$$
$$dM_{zp}/dt = -\gamma B_1 M_{yp}$$

These equations can now be combined in one simple equation of motion:

$$d\boldsymbol{M}_p/dt = \gamma \boldsymbol{M}_p \times \boldsymbol{B}_{eff} \qquad \text{(A-20)}$$

where

$$\boldsymbol{B}_{eff} = B_1 \hat{i}_p + (B_0 + \omega/\gamma)\hat{k}_p \qquad \text{(A-21)}$$

The resulting equation of motion in the rotating frame is of the same form as the one in the laboratory frame Eq. A-15. The major difference is the presence of the effective time-dependent magnetic field $\boldsymbol{B}_{eff}$ instead of $\boldsymbol{B}$. $\boldsymbol{B}_{eff}$ also has components in the x and z directions implying that the magnetization vector will precess in a cone about the $\boldsymbol{B}_{eff}$ axis with frequency $\omega_{eff} = \gamma B_{eff}$ in the laboratory frame.

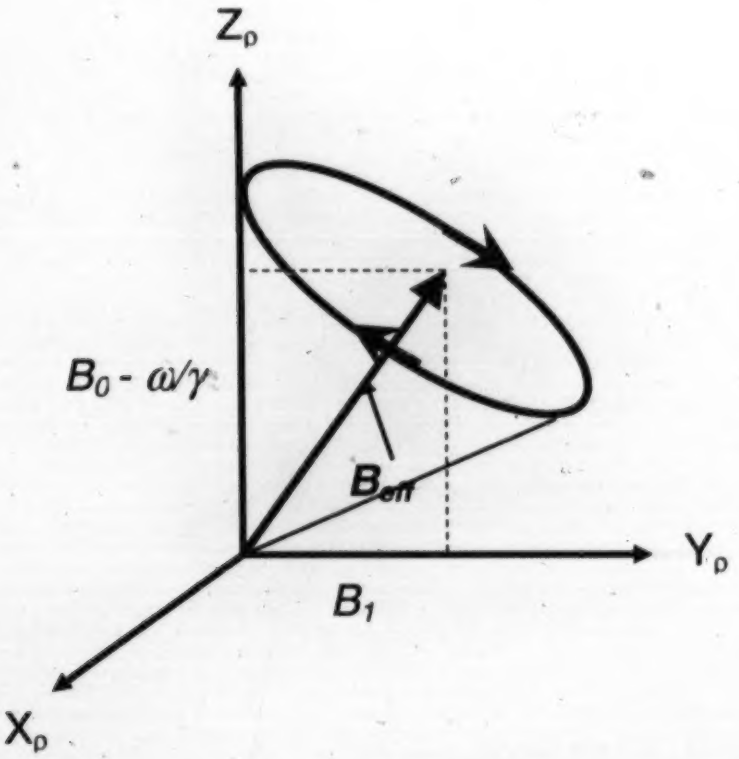

Figure (A-4): The magnetization vector precession about B_{eff} in the rotating reference frame.

From Eq. A-21, if $\boldsymbol{B_1}$ is applied so that $\omega = -\gamma B_0$, B_o is eliminated from the equation and $\boldsymbol{B_{eff}}$ becomes equal to $\boldsymbol{B_1}$. This is referred to as the resonance condition. Accordingly, if $\boldsymbol{B_1}$ is applied parallel to the x_ρ-axis the magnetization vector will precess in a circular motion in the $z_\rho y_\rho$-plane. Thus, excitation is achieved by applying a circularly polarized magnetic field $\boldsymbol{B_1}$ for a time t which will in turn cause the magnetization vector to tip from the equilibrium position along the z-axis to the transverse plane giving resulting in a detectable signal.[4]

The angle between the magnetization vector and the z-axis resulting from an excitation pulse is known as the flip angle which is defined as:

$$\alpha(t) = \gamma \int B_1(t) dt \qquad \text{(A-22)}$$

Accordingly, if $\boldsymbol{B_1}$ is applied for time $t = \pi/2\gamma B_1$ the resulting flip angle would be $\pi/2$ which is know as a 90° flip angle (pulse). Similarly, $t = \pi/\gamma B_1$ results in a 180° flip angle (pulse).

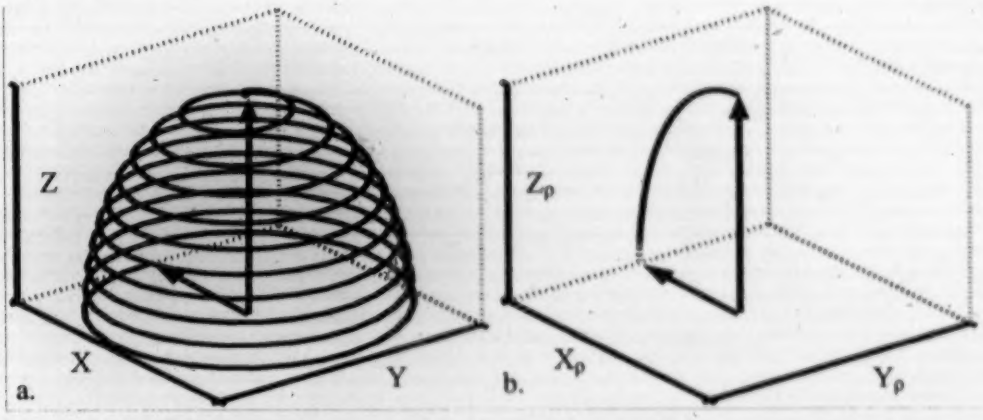

Figure (A-5): The motion of the magnetization vector during a 90° excitation pulse shown in a. the laboratory frame and b. the rotating frame.

In the laboratory frame, after excitation, the magnetization vector may have a longitudinal component M_z along the z-axis and a transverse component M_{xy} in the xy-plane. After excitation, $\boldsymbol{B_1}$ is turned off and the magnetization vector is now under the influence of only on magnetic field $\boldsymbol{B_0}$.

Description of the signal-inducing excited state:

In the excitation stage the magnetization vector $\boldsymbol{M}$ is tipped from the z-axis (axis of $\boldsymbol{B_0}$) creating a transverse component of $\boldsymbol{M}$. The transverse component is described here in complex form as:

$$\boldsymbol{M}_{xy} = (M_x, M_y, 0) = M_x + iM_y \qquad \text{(A-23)}$$

where, $i = \sqrt{-1}$.

The equations of motion for the transverse moment vectors can be expressed by equating the rate of change of angular momentum to the torque experienced by those moment vectors.[7]

$$h d\boldsymbol{I} / dt = \boldsymbol{\mu} \times \boldsymbol{B}_0 \qquad \text{(A-24)}$$

From Eq. A-1, we obtain:

$$d\boldsymbol{\mu} / dt = \gamma \boldsymbol{\mu} \times \boldsymbol{B}_0 \qquad \text{(A-25)}$$

From Eq. A-10 the equation of motion now becomes:

$$\frac{d}{dt}(\sum \boldsymbol{\mu}_{xy}) = d\boldsymbol{M}_{xy} / dt = \gamma \sum \boldsymbol{\mu}_{xy} \times \boldsymbol{B}_0$$

$$dM_{xy}/dt = \gamma M_{xy} \times B_0 \tag{A-26}$$

$$dM_{xy}/dt = \gamma \begin{vmatrix} \hat{i} & \hat{j} & \hat{k} \\ M_x & M_y & 0 \\ 0 & 0 & B_0 \end{vmatrix} = \gamma(M_y B_0 \hat{i} - M_x B_0 \hat{j}), \tag{A-27}$$

or, in complex form,:

$$\begin{aligned} dM_{xy}/dt &= \gamma M_y B_0 + i(-M_x B_0) \\ dM_{xy}/dt &= \gamma B_0 (M_y - iM_x) \\ dM_{xy}/dt &= -i\gamma B_0 M_{xy} \end{aligned} \tag{A-28}$$

Solving the differential equation above with the initial condition that $M_{xy} = iM_0$ at t = 0:

$$M_{xy}(t) = iM_0 \exp(-i\gamma B_0 t) \tag{A-29}$$

Thus the magnetization vector precesses around the z-axis with frequency $\omega_0 = \gamma B_0$. The rotation is in the negative sense for protons where γ is positive. It is important to note that the M_{xy} rotates about the z-axis in the same manner and frequency required to achieve the on-resonance excitation described in the previous section.

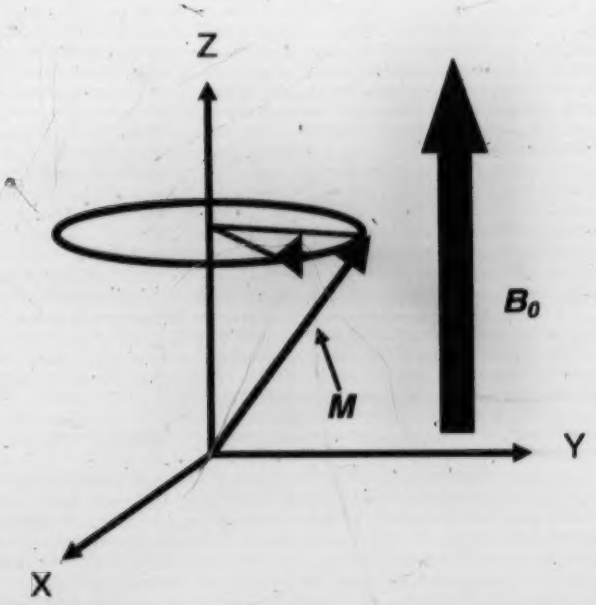

Figure (A-6): Magnetization vector M_0 precessing in a negative sense about the z-axis in the presence of a static magnetic field B_0 applied along the z-direction.

By placing an antenna adjacent to our excited sample, the rotating magnetization vector would induce a current in the conductor resulting in the detection of the signal.[1] The Fourier transform of the detected current is a peak at the resonance frequency ω_0 of the magnetization vector. (Fig. A-7)

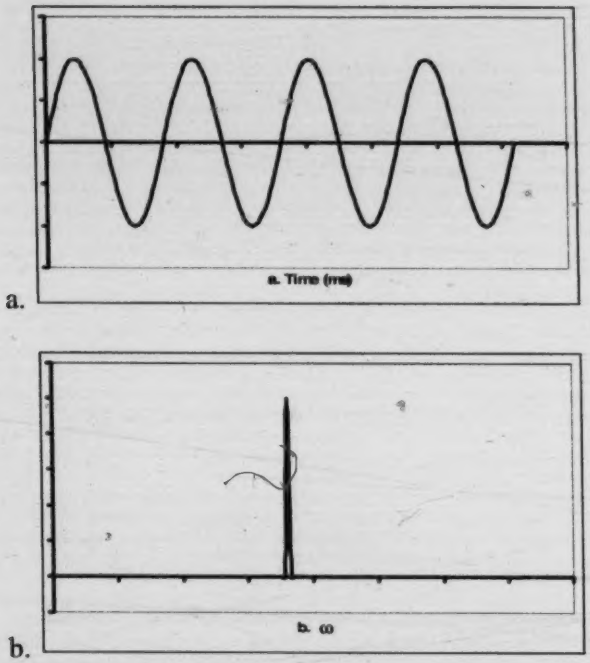

Figure (A-7): a. the time domain induced e.m.f in the coil and b. frequency profile of the detected signal. (Ignoring relaxation)

Relaxation mechanisms and the Bloch equations:

The magnetic moments represented by the magnetization vector $\boldsymbol{M}$ do not revolve indefinitely around the z-axis after excitation. Magnetic moments tend to relax to their equilibrium state along the z-axis resulting in a reduction in the measurable signal over time. The relaxation process is controlled by two related processes of longitudinal and transverse relaxation.

Longitudinal relaxation:

Longitudinal relaxation describes the change of the $\boldsymbol{M_z}$ component of the magnetization vector $\boldsymbol{M}$ from the excited state to its thermal equilibrium state $\boldsymbol{M_0}$.

Longitudinal relaxation is also known as *T1* relaxation where the longitudinal relaxation time is $T1 = 1/k$ and k is the relaxation constant. Longitudinal relaxation occurs through spin-lattice interactions where energy is exchanged between the resonant nuclei and the surrounding molecular lattice. Any one proton in a sample is closely surrounded by similar magnetic dipoles giving rise to inter-nuclear dipole fields of the same order of magnitude of $\boldsymbol{B}_1$ used in the excitation stage. Those microscopic magnetic fields are randomly changing due to the motion of the dipole lattice. Such change results in energy exchange between the spins and the lattice.

The energy exchange rates depend on the molecular lattice, accordingly, different materials exhibit different exchange rate. Bloch and Purcell, in independent accounts, showed that the longitudinal relaxation rate was proportional to the degree by which the magnetic moments have been removed from the thermal equilibrium state.[5, 6] Thus, the change in longitudinal component of the magnetization vector is expressed as:

$$dM_z(t)/dt = \frac{1}{T1}(M_0 - M_z(t)) \qquad \text{(A-27)}$$

where M_0 is the thermal equilibrium state magnetization and *T1* is the longitudinal relaxation time, a constant that that varies for different materials. The first order differential equation gives:

$$M_z(t) = M_0 + (M_z(0) - M_0)e^{-t/T1} \qquad \text{(A-28)}$$

For a 90° pulse, $M_z(t)$ becomes:

$$M_z(t) = M_0(1 - e^{-t/T1}) \qquad \text{(A-29)}$$

and for a 180° pulse:

$$M_z(t) = M_0(1 - 2e^{-t/T1}) \qquad \text{(A-30)}$$

Table A-1 shows different *T1* values for different tissue at both 1.5T and 3.0T.[3, 7] Contrast between tissue can be obtained through the choice of an appropriate timing as shown in Fig. A-8 and Fig. A-9.

Tissue	T1 (ms) @ 1.5 Tesla	T1 (ms) @ 3.0 Tesla
White Matter	790	850
Grey Matter	920	1300
Cerebrospinal Fluid (CSF)	> 4000	> 4000
Muscle	870	1073
Fat	250	419

Table (A-1): T1 value of different tissue at 1.5T and 3T.

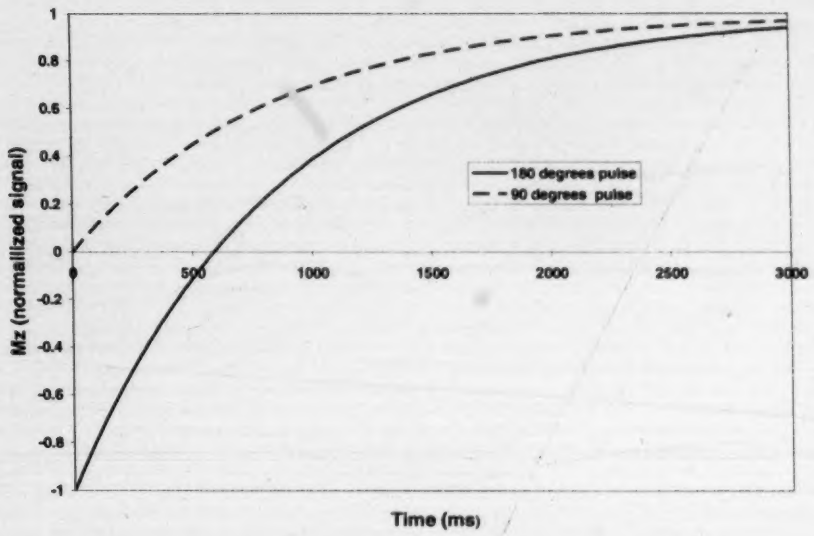

Figure (A-8): longitudinal relaxation of white matter at 3T following a 90° pulse and a 180° pulse.

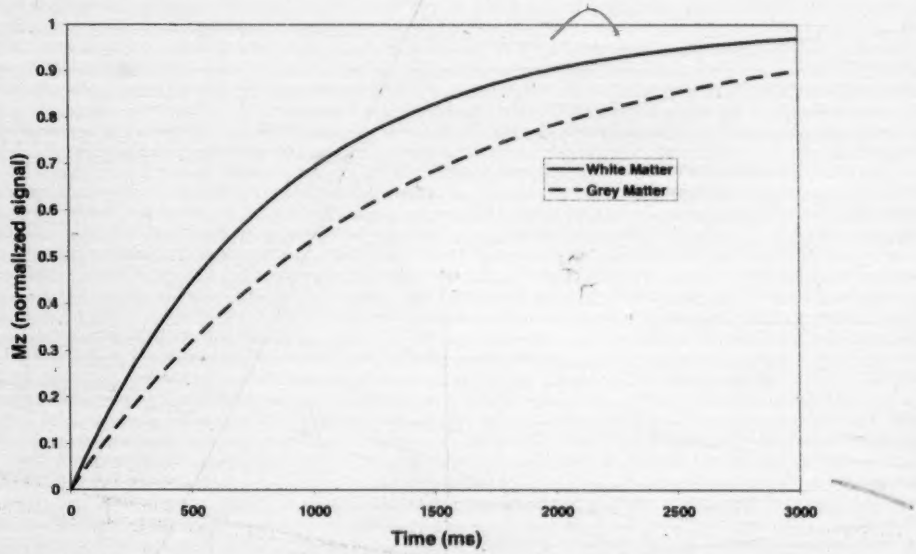

Figure (A-9): longitudinal relaxation of white matter and grey matter at 3T following a 90° pulse.

Transverse Relaxation:

Transverse relaxation describes the decay of the M_{xy} component of the magnetization vector M from its excited state back to its thermal equilibrium state. Transverse magnetization is more complicated than longitudinal relaxation as it is composed of two processes, a reversible and an irreversible process.

Similar to longitudinal relaxation, transverse relaxation is governed by a relaxation constant k', where the transverse relaxation time $T2^* = 1/k'$. The reversible and irreversible components of relaxation define $T2^*$ as [2]:

$$\frac{1}{T2^*} = \frac{1}{T2} + \frac{1}{T2'} \tag{A-31}$$

where $T2$ and $T2'$ are the irreversible and reversible components respectively. Similar to Eq. A-27, the rate of change of M_{xy} is expressed as:

$$dM_{xy}(t)/dt = \frac{1}{T2^*}(0 - M_{xy}(t)) \tag{A-32}$$

The first order differential equation gives:

$$M_{xy}(t) = M_{xy_0} e^{-t/T2^*} \tag{A-33}$$

The irreversible component *T2* results from several factors.[8] Among the various factors is the spin-spin interaction which is similar to the same mechanism of longitudinal relaxation. In spin-spin interactions, an excited dipole produces magnetic field similar in effect to $\boldsymbol{B_1}$ and excites the surrounding dipole moments. Fluctuation of the resonance frequency ω_0 due to molecular vibrations and rotations also contributes to *T2*. Those fluctuations result in the loss of coherence in the detected signal.(Fig. A-10) From its name, irreversible decay results in permanent signal loss. Table A-2 shows typical *T2* times at 1.5 T.

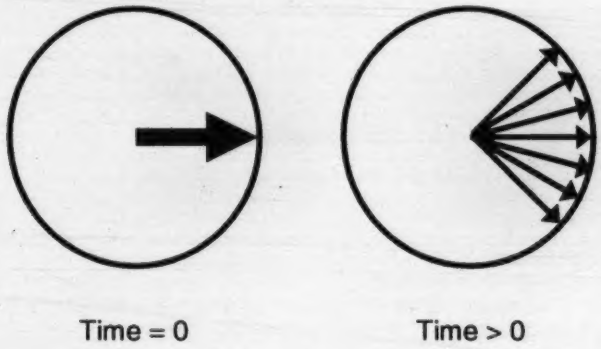

Figure (A-10): Fluctuations in ω_0 resulting in phase spread and loss of coherent signal.

Tissue	T2 (ms)
White Matter	92
Grey Matter	100
Muscle	470

Table (A-2): T2 values for brain tissue at 1.5 T.

The reversible component $T2'$ arises from the inhomogeneity in the main static magnetic field $\boldsymbol{B_0}$. Due to manufacturing imperfections in the hardware and local sources of magnetism within the sample, not all protons experience the same magnetic field $\boldsymbol{B_0}$. However, this decay component can be reversed using echoes as we will show later.

Spatial Encoding:

Spatial encoding is the process by which the signal received in an NMR experiment is related to the location it corresponds to within the anatomy. Spatial encoding distinguishes MRI from any NMR experiment. The Imaging in Magnetic Resonance Imaging comes from the ability to correlate physical location with the signal received, which is achieved by spatial encoding. To do this, a linearly varying magnetic field gradient with slope $\boldsymbol{G_r}$ is applied along the direction of the main field $\boldsymbol{B_0}$ resulting in a spatial varying $\boldsymbol{B_{total}}$:

$$B_{total} = B_0 + \boldsymbol{G_r} \bullet \boldsymbol{r} \qquad \text{(A-34)}$$

where $\boldsymbol{r}$ is the displacement along the direction of the gradient $\boldsymbol{G_r}$. (Fig. A-11) The resonance frequency now becomes linearly varying as:

$$\omega_{total} = \gamma(B_0 + \boldsymbol{G_r} \bullet \boldsymbol{r}) \qquad \text{(A-35)}$$

In the rotating frame Eq. A-33 becomes:

$$\omega_\rho = \omega(r) = \gamma G_r \bullet r \qquad \text{(A-36)}$$

Equation A-36 is the basis for the spatial encoding used in three ways in MRI as described in the following sections.

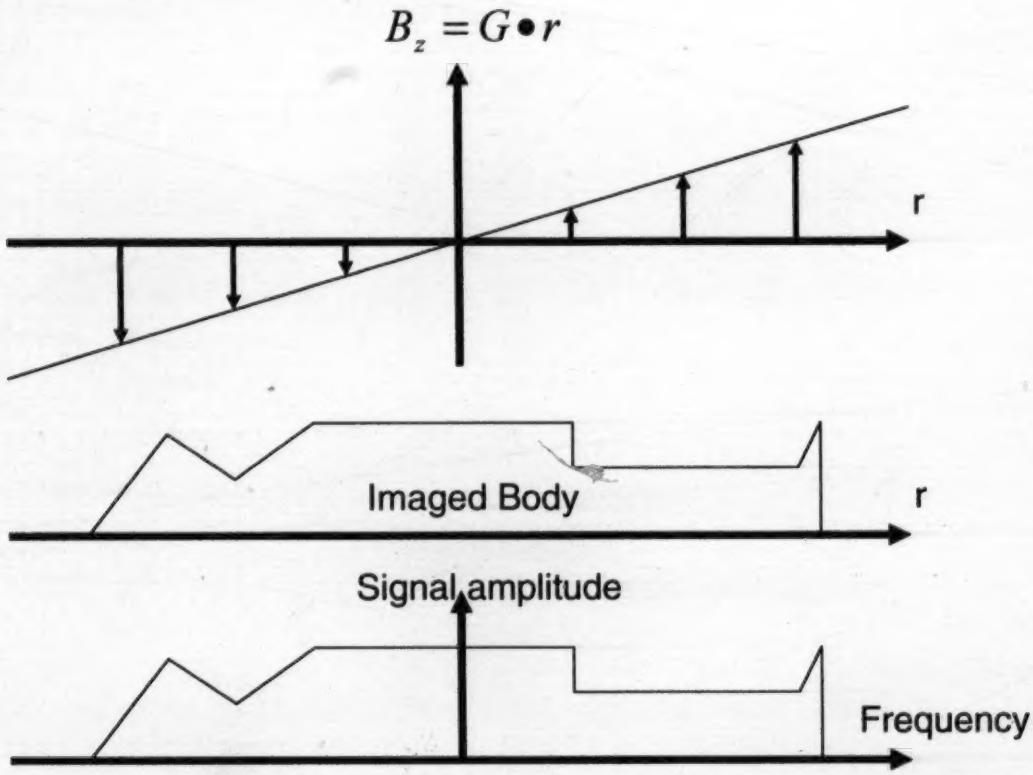

Figure (A-11): A description of the application of magnetic field gradients for spatial encoding.

Spatial encoding is achieved using primarily three methods; slice selection, frequency encoding, and phase encoding. Each of those methods makes use of the

magnetic field gradients to either limit the excitation to a certain region of the object or to spatially encode the excited volume into smaller voxels.

Slice Selection:

In slice selection, the pulse used to excite the spins is a shaped RF envelope with bandwidth BW_{rf}. A gradient G_z is applied simultaneously with the bandwidth limited RF pulse resulting in the spreading the resonance frequencies of the spins along the direction of the gradient. The RF pulse therefore excites the spins whose resonance frequencies lie within the bandwidth of the pulse.[9] Hence:

$$BW_{rf} = \gamma G_z \Delta z / 2\pi$$
$$\Delta z = 2\pi BW_{rf} / \gamma G_z \qquad \text{(A-37)}$$

where Δz is the slice thickness. The slice location can be changed by changing the center frequency of the RF pulse.

Frequency Encoding:

In frequency encoding, a gradient G_x is applied during the acquisition of the signal. As in slice selection, the gradient has the effect of spreading the resonance frequencies of the spins along the direction of the gradient. In turn this leads to a frequency spread in the acquired signal. By Fourier transform, the time domain signal is transformed into its frequency components which are directly related to the spatial locations along G_x. The range of frequencies in the acquired signal is:

$$\Delta f_{max} = \gamma G_x (x_{max} - x_{min}) / 2\pi = \gamma G_x FOV_x / 2\pi \quad \text{(A-38)}$$

where FOV_x is the field-of-view in the x-direction and is equal to $(x_{max}-x_{min})$.

The maximum frequency in the acquired signal is predictable and defined as:

$$f_{max} = \gamma G_x FOV_x / 4\pi \quad \text{(A-39)}$$

According to the Nyquist criteria, to avoid aliasing, the sampling frequency of the acquired signal must be greater than or equal to twice the maximum frequency of the signal. Hence, the sampling bandwidth of the readout gradient must be:

$$BW_{sam} \geq \gamma G_x FOV / 2\pi \quad \text{(A-40)}$$

Aliasing is usually eliminated in scanners by using a filter that only allows the frequencies within the acquisition sampling bandwidth.

Spatial resolution in the frequency encoding direction is given by:

$$\Delta x = FOV_x / N_F \quad \text{(A-41)}$$

where Δx is the pixel size in the frequency encoding direction and N_F is the number of sampling points of the readout acquisition.

Phase Encoding:

Phase encoding is similar to frequency encoding in that it uses gradients and accumulating phase to encode for the y-direction. A gradient G_y is switched on for a fixed time τ before acquisition. This results in the accumulation of phase that is linear with the position along the phase encoding direction. Accordingly, at the start of the acquisition the all spins have the same resonance frequency but with phase spread linearly along the y-direction.

$$\phi(y) = \gamma \int_{\tau} G_y(t) \bullet y dt \qquad \text{(A-42)}$$

where ϕ is the phase accumulated before acquisition.

That gradient strength is then incremented by discrete linear increments of ΔG_y before each acquisition. This results in a distribution of phase along the phase encoding direction which resembles pseudo-frequencies that are linearly related to the spins' y location.

The maximum phase shift between two adjacent points is given by:

$$\Delta\phi_{max} = 2\pi f_{max}\tau = \gamma\tau\Delta G_y FOV_y / 2 \qquad \text{(A-43)}$$

where FOV_y is the field-of-view in the phase encoding direction.

Similar to frequency encoding, to satisfy the Nyquist criteria the maximum phase shift between adjacent samples must be less than or equal to π The gradient increments than have to be:

$$\gamma\tau\Delta G_y FOV_y / 2 \le \pi$$
$$\Delta G_y \le 2\pi / (\gamma FOV_y \tau) \qquad \text{(A-44)}$$

Similar to Eq. A-41, the spatial resolution in the phase encode direction is given by:

$$\Delta y = FOV_y / N_p \qquad \text{(A-45)}$$

where Δy is the pixel size in the phase encoding direction and N_p is the number of phase encode steps in the y-direction.

Radio-Frequency excitation pulses:

Recall the slice selection section, we briefly discussed the application of an RF pulse along with a slice selection gradient to excite a slice from our imaging body. It is the frequency profile of the RF pulse that we are interested in. Equation A-37 shows that as the slice selection gradient spreads the frequencies of the spins over a certain range, the bandwidth of the RF pulse is the limiting factor of the slice thickness. The frequency profile of an RF pulse is simply the Fourier transform of the time domain pulse signal. The bandwidth of the pulse (BW_{rf}) is defined as the full width at half maximum of that power spectrum.

Two of the basic RF pulses used in MRI are hard and soft pulses. Hard pulses are square pulses in the time domain and have a corresponding sinc function frequency profile. Hard pulses have the advantage of achieving large tip angles in a very short time. However, due to its frequency profile, it is considered a broadband pulse that results in poor slice definition.(Fig. A-12) The side lobes in the frequency profile of the pulse lead to contamination of signal of the slice with signal from neighboring slices.

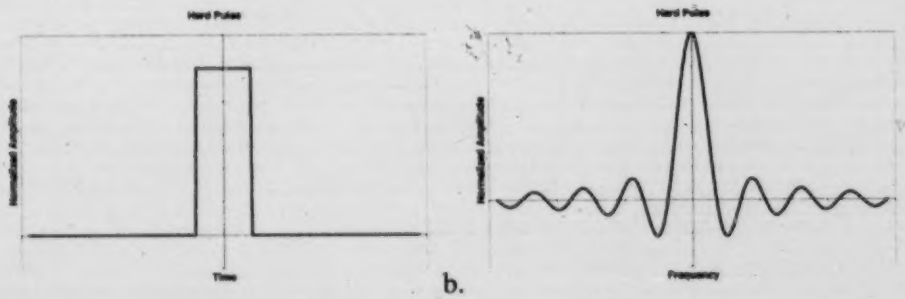

a. b.

Figure (A-12): A typical hard pulse as shown in a. time domain and b. frequency domain.

Soft pulses on the other hand, are truncated sinc pulses in the time domain with a corresponding approximately square frequency profile.[10] Although, soft pulses have a relatively long play time, the resulting frequency response get sharper and better defined with greater time lengths. It is a trait that is sought for in imaging since it provides sharply defined slices as shown in Fig. A-13.

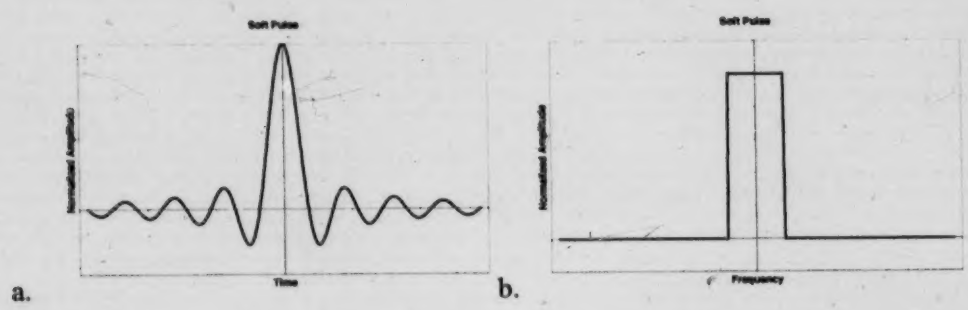

a. b.

Figure (A-13): An ideal soft pulse as shown in a. time domain and b. frequency domain.

The latter observation is true for all pulses. As a general rule of thumb, the time domain play time and frequency domain bandwidth are inversely proportional. This means that the narrower the time domain profile of a pulse is, the wider its frequency profile and visa-versa.

The Signal Equation:

The focus of this section is to discuss the signal received after excitation and encode and how this signal is processed to give us the image we desire. For simplicity we will consider a basic two-dimensional sequence which resulting signal is detected by a phase sensitive detector. We shall also ignore *T2* relaxation for the time being.

In the selectively excited slice, the receiving coil detects the signal from all the precessing spins. The sum of the received signal from the magnetization vector M_{xy} can be written as an integral:[7]

$$S(t) = \int_x \int_y M(x,y) \exp[-i\gamma(\int_0^t G_x(\tau)d\tau - i\gamma\int_0^t G_x(\tau)d\tau]dydx \qquad \text{(A-46)}$$

Consider defining a new variable k where:

$$k_x(t) = \gamma\int_0^t G_x(\tau)d\tau$$
$$\text{(A-47)}$$
$$k_y(t) = \gamma\int_0^t G_y(\tau)d\tau$$

Substituting with Eq. A-47 in Eq. A-46:

$$S(t) = \int_x \int_y M(x,y)e^{-i(k_x(t)x+k_y(t)y)}dydx \qquad \text{(A-48)}$$

It is very important to notice the similarity between Eq. A-49 and the definition of the Fourier transform.[11] Such similarity allows us to reconstruct the distribution of the signal in the form of an image using 2-D inverse Fourier transform.

The introduction of the terms k_x and k_y in our discussion lead to questions about their significance. k_x and k_y are components in k-space in which frequency and phase replace the normally understood displacement real space. For instance if an MRI image is Fourier transformed in 2 dimensions, the resulting would be an image with the same number of points but in k-space. Thus, in order to correctly acquire a complete high-resolution image, all k-space points of the image have to be correctly

sampled. As it has been described before and through Eq. A-48 this is achieved through the application of gradients in the frequency and phase encoding.

Consider a 2D gradient echo sequence. We shall discuss how this sequence samples k-space. As in Fig. A-14 the sequence is divided into time *t1* and time *t2*. During *t1,* the phase encode gradient and negative half readout gradient are on. Both gradients result in a shift the k-space coordinates to (k_x1, k_y1). For a time *t2* the frequency encode (readout) gradient is not turned on and the signal is acquired leading to a precession of the coordinates through a row of k_x in k-space.[7] In the next acquisition, the same steps are repeated but with incrementing the phase encode gradient G_y by ΔG_y. This results in sampling another row of k-space. This process is repeated until al k-space is properly sampled.

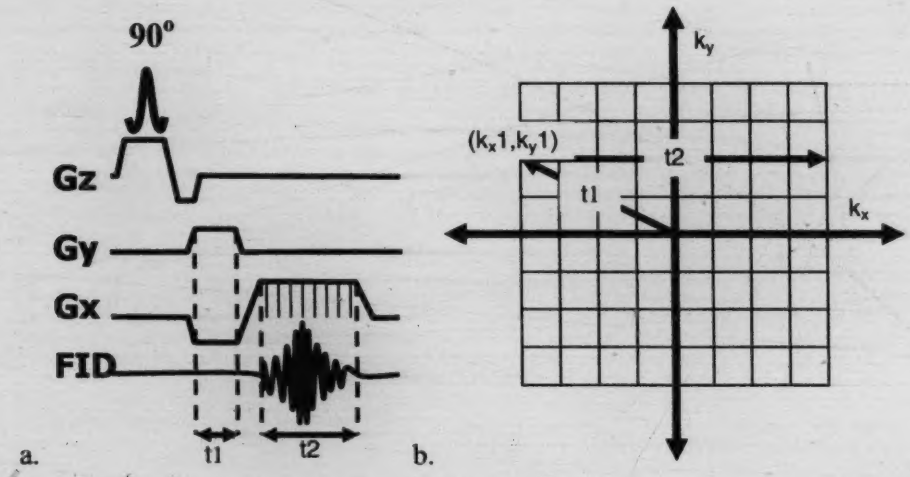

Figure (A-14): a. schematic of a gradient echo sequence. b. the k-space sampling trajectory caused by the application of the gradients in the sequence.

There are of course several ways in which k-space can be sampled each with its pros and cons and it is generally a process optimized for each application.[2, 3, 12]

According to the sampling theory, sampling in one domain corresponds to replication in the corresponding transform domain.[7] Since, in MR sampling is done in k-space, the replication of the image must be considered. Replication occurs at intervals of $1/\Delta k_x$ and $1/\Delta k_y$ in the x and y directions respectively.[7] The field of view is therefore related to the k-space sampling rate through:

$$FOV_x = 1/\Delta k_x = \frac{1}{\gamma G_x \Delta t} = sampling\ rate\ in\ k_x \qquad \text{(A-59)}$$

$$FOV_y = 1/\Delta k_y = \frac{1}{\gamma \Delta G_y \tau} = sampling\ rate\ in\ k_y \qquad \text{(A-50)}$$

From Eq. A-41, and Eq. A-45 we obtain:

$$\begin{aligned} \Delta x &= FOV_x / N_F = 1/\Delta k_x N_F \\ \Delta y &= FOV_y / N_P = 1/\Delta k_y N_P \end{aligned} \qquad \text{(A-51)}$$

Therefore, the in-plane voxel dimensions are inversely proportional to the extent of k-space.

References:

1. Bronskill, M.J. *The physics of MRI.* in *AAPM summer school proceeding.* 1992 Woodbury: American Institute of Physics, Inc.
2. Haacke, E.M., *Magnetic Resonance Imgaing, physics principles and sequence design.* 1999: John Willey & Sons.

3. Thomas, S.D., *Transient magnetization MRA at 3.0 Tesla*, in *Biomedical Engineering*. 2001, University of Alberta: Edmonton.
4. Hinshaw, W.S. *An introduction to NMR imaging.* in *Proceeding of the IEEE.* 1983.
5. Block, F., *Nuclear induction.* Physical Review, 1946. **70**: p. 460-474.
6. Purcell, E.M., Torrey, H.C., Pound, R.B., *Resonance absorption by nuclear magnetic moments in a solid.* Physical Review, 1946. **69**: p. 37-38.
7. Nishimura, D.G., *Principles of Magnetic Resonance Imaging*. 1996: Stanford University.
8. Brown, M.A., Semelka, R.C., *MRI Basic Principles and Applications.* 1995: John Wiley & Sons.
9. McRobbie, D.W., *Investigation of the slice characteristics in NMR imaging.* Phys. Med. Biol., 1986. **31**(6): p. 613-626.
10. Freeman, R., *Shaped freuqncy pulses in high resolution NMR.* J. of Progress in NMR Spectroscopy, 1998. **32**: p. 59-106.
11. Bracewell, R.N., *The Fourier Transform and its Applications.* 1978: McGraw-Hill. 122.
12. Bishop, J., Plewes, D. *Stimulated echo effects in fast spin echo images.* in *10th Annual Mtg. Soc. Magn. Reson. In Med.* 1991. San Francisco.

Appendix II: Peak Fitting Algorithm

The following programs were written in MATLAB v. 6.5.2. Where the lines starting with (%) are comment lines.

```
%Least Square fitting of the FWHM (ai) and phase angle (phi) for the
%Cho and Cr peaks

Param = fminunc(@ls_sq, [ai; phi]);

%%%%%%%%%%%%%%%%%%%%%%%%%%%%%%%%%%%%%%%%%%%%%%%%%%%%%%%%%%%%%%%%%%%%%%%%%%%


%The function that calculates:
%     1. The sum of lorentzians for a specified %
%     number of peak.
%     2. The sum of squares of the difference between the raw
%     spectrum and the sum of lozentzians fit.

function F = ls_sq(x)
v = [Xavg(1): Xavg(2), Xavg(3):Xavg(4)]; % Peak fitting windows

%Calculation of the lorentzians (Cho and Cr)
for ii = 1:2
FL(ii, :, :) = [(x(1,ii).^2*Ii(ii)./(x(1,ii).^2+4*(v-vi(ii)).^2))'…
     …-(2*x(1,ii).*Ii(ii)*(v-vi(ii))./(x(1,ii).^2+4*…
     …(v-vi(ii)).^2))'] *[cos(x(2,ii)) sin(x(2,ii)); -sin(x(2,ii))…
     …cos(x(2,ii))];
FL_comp(ii,:) =squeeze(FL(ii,:,1) + i*FL(ii,:,2));
end

%Calculation of the sum of lorentzians of Cho and Cr
FLor_sum = FL_comp(1,:) + FL_comp(2,:);

%Calculation of the sum of squares of the difference between the raw
%spectrum and the sum of lorentzians fit
F = sum((real(D_smooth(v,sx,sy))'-real(FLor_sum)).^2);

%%%%%%%%%%%%%%%%%%%%%%%%%%%%%%%%%%%%%%%%%%%%%%%%%%%%%%%%%%%%%%%%%%%%%%%%%%%
```